8-6-2005

First-Principles Study Of Semiconductor And Metal Surfaces

Sungho Kim

Recommended Citation

Kim, Sungho, "First-Principles Study Of Semiconductor And Metal Surfaces" (2005). *Theses and Dissertations*. 2302.
https://scholarsjunction.msstate.edu/td/2302

FIRST-PRINCIPLES STUDY OF SEMICONDUCTOR AND METAL SURFACES

By

Sungho Kim

A Dissertation
Submitted to the Faculty of
Mississippi State University
in Partial Fulfillment of the Requirements
for the Degree of Doctor of Philosophy
in Engineering Physics
in the Department of Physics and Astronomy

Mississippi State, Mississippi

August 2005

FIRST-PRINCIPLES STUDY OF SEMICONDUCTOR AND METAL SURFACES

By

Sungho Kim

Approved:

Seong-Gon Kim
Assistant Professor of Physics and Astronomy
(Major Professor)

John T. Foley
Professor of Physics and Astronomy
(Committee Member)

Henk F. Arnoldus
Associate Professor of Physics and Astronomy
(Committee Member)

R. Rainey Little
Associate Professor of
Computer Science and Engineering
(Committee Member)

Vivien G. Miller
Associate Professor of Mathematics
(Committee Member)

Thomas Philip
Professor of Computer Science and Engineering
(Committee Member)

Kirk Schulz
Dean of the Bagley College of Engineering

Name: Sungho Kim

Date of Degree: August 6, 2005

Institution: Mississippi State University

Major Field: Engineering Physics

Major Professor: Dr. Seong-Gon Kim

Title of Study: FIRST-PRINCIPLES STUDY OF SEMICONDUCTOR AND METAL SURFACES

Pages in Study: 95

Candidate for Degree of Doctor of Philosophy

In this dissertation, we study the electronic and geometric structure of semiconductors and metal surfaces based on quantum mechanical first-principles calculations.

We determine the geometry of vacancy defects of hydrogen adsorbed on a Pd(111) surface by treating the motion of a hydrogen atom, in addition to electrons, quantum mechanically. The calculated ground state wave function has high probability density in the hcp site located at the center of the vacancy instead of the fcc sites where the potential is minimum and hydrogen atoms on a Pd(111) surface normally adsorb. The geometry of quantum mechanically determined divacancy provides a simple and clear explanation for the scanning tunneling microscopy (STM) images of these defects that appear as three-lobed objects as observed in recent experiments [Mitsui, *et al*, Nature 422, 705 (2003)]. We employ the same principle to successfully elucidate the STM images of larger size vacancy defects. Our model also provides a compelling argument to explain the unusual

recent experimental result that aggregates of three or more hydrogen vacancies are much more active in adsorption of hydrogen molecules while two-vacancy defects are never inactive.

The InAs (110) surfaces appear lower than GaSb in STM images. This height difference is caused primarily by differences in the electronic structure of the two materials according to our calculations in a good agreement with measurements. In contrast, local variations in the apparent height of (110) surface atoms at InSb- or GaAs-like interfaces arise primarily from geometric distortions associated with local differences in bond length. The arsenic atoms adsorb preferably at the bridge sites between the dimerized Sb atoms on Sb-terminating (001) surfaces. Indium atoms, on the other hand, have somewhat equal probabilities at a few different sites on Ga-terminating (001) surfaces. Our calculated energies for atomic intermixing indicate that anion exchanges are exothermic for As atoms on Ga-terminating (001) interfaces but endothermic for In atoms on Sb-terminating (001) interfaces. This difference may explain why GaAs interfaces are typically more disordered than InSb interfaces in these heterostructures.

ACKNOWLEDGMENTS

First and foremost, I would like to thank my supervisor, Dr. Seong-Gon Kim, for his thoughtful guidance and introducing the interesting research field. Without his extensive help this dissertation would have taken far longer to complete. I thank Dr. Henk F. Arnoldus for giving me chance to come out to bigger world and supporting me sincerely since beginning.

This work was done by using ERC supercomputer facility, without which this work would not have been possible.

I thank my wife, Sunmi Jin, for her love and dedication to me.

TABLE OF CONTENTS

Page

CHAPTER

LIST OF TABLES

LIST OF FIGURES

CHAPTER I

INTRODUCTION

The formulation and development of quantum theory in the first half of the 20th century has led to a revolution in our understanding of fundamental physics. Quantum theory has demonstrated a surprising accuracy and predictive power, and the importance of quantum theory in the pure and applied sciences is virtually unchallenged. If we are to attempt to model real processes and real materials the relevant equation to be solved is clearly the Schrödinger equation. Unfortunately, however, the Schrödinger equation cannot be solved analytically for any practical system but a few trivial ones. In order to make useful progress the Schrödinger equation must be solved numerically with rigorously controlled approximations.

Density functional theory (DFT) [62, 48, 52, 40] is widely used in condensed matter physics and computational chemistry. DFT provides a formal foundation that the total energy of many-electron system is a unique functional of the electron density[62]. Furthermore, Kohn-Sham theory allows us to replace the many-electron problem by a set of Schrödinger-like self-consistent single-electron equations[48].

We use DFT to study metal surfaces and their interaction with adsorbates. In particular, we determine the ground-state geometry of vacancy defects of H atoms adsorbed on

Pd(111) surface. Due to special circumstances in the vicinity of these defects, H atoms need to be treated fully quantum mechanically to obtain correct ground-state geometry of these defects and the results explain many unexpected and yet interesting experimental observations. Therefore, we go beyond conventional DFT methods employed in condensed matter physics and developed our own new software package to obtain the quantum mechanical behavior of H atoms as well as electrons.

We also apply first-principle calculations based on density functional theory to study the surface of various semiconductors. In particular, we determine the structure of interfaces between several III-V heterostructure semiconductors such as GaAs, GaSb, InAs, and InSb.

1.1 Overview

The dissertation is organized as follows. In Chapter 2, we review the fundamentals of the density functional theory introduced by Hohenberg, Kohn and Sham during the sixties. In Chapter 3, we describe how we treat hydrogen atom quantum mechanically on Pd(111) surface and introduce the program APPSES we developed. In Chapter 4, first-principles study of metal surfaces is presented. In Chapter 5, first-principles study of semiconductor surfaces is presented.

CHAPTER II

DENSITY FUNCTIONAL THEORY

Density functional theory (DFT) is widely used in condensed matter physics and, due to its tremendous success, is emerging as a de facto standard to solve many-body problem of electrons in atomic scale systems [62, 48, 52, 40]. The Born-Oppenheimer approximation, discussed in Section 2.1, is used to separate the dynamics of the ions from the electrons. DFT is motivated by the Hohenberg-Kohn (HK) theorem[62], derived in Section 2.2, which maps the N-interacting electron problem into a variational problem cast in terms of the ground state single particle density $\rho(\mathbf{r})$. The Kohn-Sham (KS) equation[48], derived in Section 2.3, describes the system in terms of a set of auxiliary functions $\{\Psi_i\}$ which are solutions to a non-linear, self-consistent single-particle Schrödinger-like equation. These variational principles provide a well-defined and well-tested means to study atomic scale systems by minimizing a total energy functional. Unfortunately, the total energy depends on an unspecified exchange-correlation energy functional E_{XC}. Despite the fact that little is known about E_{XC}, well-controlled approximations to E_{XC} have been surprisingly successful and have been applied to a wide range of systems. An overview of E_{XC} functionals in popular use is given in Section 2.4. To a large extent, the properties of an atomic system are determined by the electrons in the valence shell of the constituent atoms. The pseudopotential approximation, described in Section 2.5, formalizes this idea by replacing the core electrons and the nucleus with a pseudopotential that describes the effective interaction of the valence and core electrons. A numerical solution of the KS-equations is based on the choice of an appropriate basis to represent the electronic wave functions. An overview of bases is given in Section 2.6. A brief description of the self-consistent solution procedure is given in Section 2.7.

2.1 Born-Oppenheimer Approximation

The ions in a solid tend to move slower than the electrons because $m_{ion} \gg m_{electron}$. In the Born-Oppenheimer approximation, the electrons are assumed to move instantaneously to their ground state and the ions can be treated as classical objects with a definite position $\mathbf{R}_K$ and velocity $\mathbf{V}_K$, experiencing a classical force $\mathbf{F}_K$ due to the potential generated by electrons and other ions. The elctrons themselves move in an external potential V_{ion-el} generated by the nuclear cores:

$$V_{ion-el}(\mathbf{r}) = \sum_K \frac{Z_K}{|\mathbf{r} - \mathbf{R}_K|}. \tag{2.1}$$

In Section 2.5, this external potential is modified to include the core states and nonclassical effects. Within this approximation, the nuclei are replaced by pseudo-ions that generate the external potential $V_{ion-el}(\mathbf{r})$.

In the Born-Oppenheimer approximation, the total energy corresponds to the energy of a system of electrons in the presence of a collection of nuclei: $E(\{\mathbf{R}_I\})$. To study an atomic scale system, it is natural to relax the ionic coordinates so that they minimize the total energy on the Born-Oppenheimer surface $E(\{\mathbf{R}_I\})$ and forces $\mathbf{F}_I = \frac{dE}{d\mathbf{R}_I}$ [23] on the ions at $\mathbf{R}_I$ disappear. These forces may be calculated *ab-initio* from the electronic ground state using the Hellman-Feynman theorem. [23, 62, 35]

There are several approaches to go beyond the Born-Oppenheimer approximation. A natural extension would be to include electron-phonon coupling. While electron-phonon coupling constants have been estimated *a posteriori* from DFT analyses [13], they have not been included in a self-consistent DFT analysis.

2.2 Hohenberg-Kohn Theorem

The basis for DFT is the Hohenberg-Kohn (HK) theorem [62] which reduces the fully interacting N-electron problem to determining the ground state of single particle density $\rho(\mathbf{r})$: *The non-degenerate ground state energy of an N electron system, E_N, is a unique, universal functional of the single-particle density $\rho(\mathbf{r})$:*

$$E_N = E_N[\rho(\mathbf{r})]. \tag{2.2}$$

This may be proven as follows. For an interacting system of electrons:

$$H = \sum_{i=1}^{N} \frac{-\nabla_i^2}{2} + \sum_{i \neq j} \frac{1}{\mathbf{r}_i - \mathbf{r}_j} + V_{ext}(\mathbf{r}) \tag{2.3}$$

The external potential $V_{ext}(\mathbf{r})$ and the number of electrons N uniquely determine the system. The density determines the number of electrons by $N = \int d\mathbf{r}\rho(\mathbf{r})$. The proof will demonstrate that there is also a one-to-one mapping between the external potential $V_{ext}(\mathbf{r})$

and the ground-state density $\rho(\mathbf{r})$. Thus, the system is uniquely determined by $\rho(\mathbf{r})$, including the wave function and total energy E_N.

Suppose there are two different potentials $V_{ext}(\mathbf{r})$ and $V_{ext}(\mathbf{r}')$ with the same ground-state density $\rho(\mathbf{r})$. These diferent potentials are associated with energies E and E', Hamiltonians H and H' and wave functions Ψ and Ψ', respectively. Using the fact that Ψ is the non-degenerate ground state of H, we obtain

$$\begin{aligned} \langle\Psi|H|\Psi\rangle &< \langle\Psi'|H|\Psi'\rangle, \\ E &< \langle\Psi'|H'|\Psi'\rangle + \langle\Psi'|H-H'|\Psi'\rangle, \\ E &< E' + \int d\mathbf{r}\rho(\mathbf{r})(V'_{ext}(\mathbf{r}) - V_{ext}(\mathbf{r})). \end{aligned}$$

Similarly,

$$\begin{aligned} \langle\Psi|H'|\Psi\rangle &< \langle\Psi|H'|\Psi\rangle, \\ E' &< \langle\Psi|H|\Psi\rangle + \langle\Psi'|H'-H|\Psi'\rangle, \\ E' &< E + \int d\mathbf{r}\rho(\mathbf{r})(V'_{ext}(\mathbf{r}) - V_{ext}(\mathbf{r})). \end{aligned}$$

Adding these two equations together results in the contradiction $E + E' < E + E'$. Thus, for a non-degenerate ground state, there cannot be two potentials $V_{ext}(\mathbf{r})$ and $V'_{ext}(\mathbf{r})$ with the same ground state density $\rho(\mathbf{r})$ and $\rho(\mathbf{r})$ uniquely determines $V_{ext}(\mathbf{r})$, N, and , consequently, all properties of the system. Although this proof was developed for a non-degenerate ground state, DFT can be formulated in such a way that the HK-theorem holds even for systems with degenerate ground states [64].

Since all properties are determined by the ground-state density, any system can be studied by minimizing a unique, universal total-energy functional $E[\rho]$. This is the motivating result of DFT. The central problem of DFT is thus to determine the form of the energy functional $E[\rho]$. Unfortunately, the exact form is not known but one can formally write

$$E[\rho] = T[\rho] + \frac{1}{2}\int d\mathbf{r}d\mathbf{r}'\frac{\rho(\mathbf{r})\rho(\mathbf{r}')}{|\mathbf{r}-\mathbf{r}'|} + \int d\mathbf{r}\rho(\mathbf{r})V_{ext}(\mathbf{r}) + E_{XC}[\rho], \tag{2.4}$$

where $T[\rho]$ is the kinetic energy and the next two terms represent the mean-field interaction energy and the energy due to the external potential, V_{ext}, respectively. All non-classical corrections and many-body effects are included in the exchange-correlation functional $E_{XC}[\rho]$. These corrections include both exchange effects (X), due to interactions between parallel spins, and correlation effects (C), due to interactions between opposite spins. In practice, one chooses among a set of standard approximate forms of $E_{XC}[\rho]$. Some popular choices are described in Section 2.4.

2.3 Kohn-Sham Equation

Many applications of DFT are based on the Kohn-Sham (KS) equations which are derive from the Hohenberg-Kohn theorem. Similar to the Hartree-Fock method, Kohn and Sham [48] introduced a non-interacting reference density built of auxiliary functions $\{\psi^i\}$:

$$\rho(\mathbf{r}) = \sum_{i=1}^{N}(\psi^i(\mathbf{r}))^*\psi^i(\mathbf{r}), \tag{2.5}$$

$$\langle\psi^i|\psi^j\rangle = \delta_{ij}. \tag{2.6}$$

The Kohn-Sham kinetic energy is given by

$$T_{KS} = \sum_{i=1}^{N} \langle \psi^i | \frac{-\delta_i^2}{2} | \psi^i \rangle. \tag{2.7}$$

The true kinetic energy $T[\rho]$ is not equal to the KS kinetic energy T_{KS}. However, this difference can again be absorbed into the exchange-correlation functional by redefining E_{XC}:

$$E_{XC}[\rho] \equiv T[\rho] - T_{KS}[\rho] + E_X[\rho] + E_C[\rho]. \tag{2.8}$$

The basic idea behind the Kohn-Sham equation is to start with a good approximation to the knetic energy, which is a large part ($\sim$ 50%) of the total energy, and absorb the presumably small non-classical correction into E_{XC}($\sim$ 10%) of the total energy[40].

In the ground state, the variation of the total energy is stationary with respect to the functions $\{\psi^i(\mathbf{r})\}$

$$\frac{\delta E[\rho]}{\delta \psi^i(\mathbf{r}')} = 0. \tag{2.9}$$

The orthogonality conditions are maintained by introducing the Lagrange multipliers E^{ij}

$$\frac{\delta E[\rho]}{\delta \psi^i(\mathbf{r}')} - E^{ij}\psi^j = 0, \tag{2.10}$$

which leads to

$$(\frac{\nabla}{2} + \int d\mathbf{r} \frac{\rho(\mathbf{r}')}{|\mathbf{r} - \mathbf{r}'|} + V_{ext}(\mathbf{r}) + V_{XC}(\mathbf{r}))\psi^i(\mathbf{r}) = E^{ij}\psi^j(\mathbf{r}), \tag{2.11}$$

where V_{XC} is the exchange-correlation potential:

$$V_{XC}[\rho)] \equiv \frac{\delta E_{XC}[\rho]}{\delta \rho(\mathbf{r})}. \tag{2.12}$$

The matrix E_{ij} can be diagonalized, leading to the Kohn-Sham equation:

$$(\frac{\nabla}{2}+\int d\mathbf{r}\frac{\rho(\mathbf{r}')}{|\mathbf{r}-\mathbf{r}'|}+V_{ext}(\mathbf{r})+V_{XC}(\mathbf{r}))\psi^{i}(\mathbf{r})=E^{i}\psi^{i}(\mathbf{r}). \tag{2.13}$$

The interacting many-electron problem has thus been reduced to a set of self-consistent one-electron (interacting with others through a mean-field potential) Schrödinger-like equations. It is emphasized that exact knowledge of the functional $E_{XC}[\rho]$ whould yield the exact ground state energy. Thus, the Kohn-Sham equations prove the existence of an exact mean field theory. However, the exact functional $V_{XC}[\rho]$ is not known and one must choose an approximate form. It is also noted that the Kohn-Sham Hamiltonian in Eq. 2.13 depends on the solutions $\{\psi^{i}\}$ through the density. The KS equations are thus a non-linear self-consistent eigenvalue problem which will require much computational effort to solve.

2.3.1 Total Energy Functional

The ground state energy can be written:

$$E_{tot}=T_{KS}+\frac{1}{2}\int d\mathbf{r}d\mathbf{r}'\frac{\rho(\mathbf{r})\rho(\mathbf{r}')}{|\mathbf{r}-\mathbf{r}'|}+\int d\mathbf{r}\rho(\mathbf{r})V_{ion-el}(\mathbf{r})+\int d\mathbf{r}\rho(\mathbf{r})V_{ext}+E_{ion-ion}[\{\mathbf{R}_I\}], \tag{2.14}$$

where we have explicitly included the external potential due to the interaction with the atomic cores V_{ion-el}. The total energy can be rewritten:

$$E_{tot}=E_{BS}-\delta E_H+\delta U_{XC}+E_{ion-ion}[\{\mathbf{R}_I\}], \tag{2.15}$$

where

$$E_{BS} = \sum_{i=1}^{N} E^{i},$$

$$\begin{aligned}\delta E_H &= -\frac{1}{2}\int d\mathbf{r}\rho(\mathbf{r})\frac{\rho(\mathbf{r})\rho(\mathbf{r}')}{|\mathbf{r}-\mathbf{r}'|},\\ \delta U_{XC} &= \int d\mathbf{r}\rho(\mathbf{r})(\frac{E_{XC}(\rho(\mathbf{r}))}{\rho(\mathbf{r})} - V_{XC}(\rho(\mathbf{r}))),\\ E_{ion-ion} &= \sum_{I\neq J}\frac{Z_I Z_J}{|\mathbf{R}_I-\mathbf{R}_J|},\end{aligned}$$

and the Kohn-Sham eigenvalues E^i are

$$E^i = \int d\mathbf{r}(\psi^i(\mathbf{r}))^*\{\frac{-\nabla^2}{2} + \int d\mathbf{r}\frac{\rho(\mathbf{r})}{|\mathbf{r}-\mathbf{r}'|} + V_{XC}(\rho(\mathbf{r}))V_{ion-el}(\mathbf{r}) + V_{ext}(\mathbf{r})\}\psi^i(\mathbf{r}). \quad (2.16)$$

There are two long-ranged potentials in the KS equations that cancel each other at large separation R:

$$V_H = \int d\mathbf{r}'\frac{\rho(\mathbf{r})}{|\mathbf{r}-\mathbf{r}'|} \sim \frac{N}{R}V_{ion-el} \sim \frac{-N}{R}. \quad (2.17)$$

These potentials may be screened by adding and subtracting the Hartree potential due to a neutral charge density $\int d\mathbf{r}\rho^{NA}(\mathbf{r}-\mathbf{R}_I) = Z_I$. This leaves a screened ion-electron interaction or neutral atom potential, V^{NA}, and a Hartree correction $V_{\delta H}$ which satisfy:

$$\nabla^2 V_{\delta H} = 4\pi[\rho(\mathbf{r}) - \sum_I \rho^{NA}(\mathbf{r}-\mathbf{R}_I)] \quad (2.18)$$

and

$$V^{NA} = \sum_K V^{NA,K}(\mathbf{r}-\mathbf{R}_K) = \sum_K\{V^K_{ion-el}(\mathbf{r}-\mathbf{R}_K) + \int d\mathbf{r}'\frac{\rho^{NA,K}(\mathbf{r}'-\mathbf{R}_K)}{|\mathbf{r}-\mathbf{r}'|}\}. \quad (2.19)$$

The KS Hamiltonian is now of the form:

$$H = \frac{-\nabla^2}{2} + \sum_K V^{NA,K}(\mathbf{r}-\mathbf{R}_K) + V_{\delta H}(\mathbf{r}) + V_{XC}(\mathbf{r}) + V_{ext}(\mathbf{r}). \quad (2.20)$$

There are also long-ranged terms in the total energy: the ion-ion interaction, $E_{ion-ion}$, and Hartree correction δE_H. These terms can again be screened by adding and subtracting $\rho^{NA}(\mathbf{r})$ so that the total energy is now written [60]:

$$E_{tot} = E_{BS} + \delta E_{\delta H} + \delta U_{XC} + E_{SR}, \tag{2.21}$$

where we have introduced the Hartree correction $\delta E_{\delta H}$

$$\delta E_{\delta H} \equiv \int d\mathbf{r} V_{\delta H}(\mathbf{r})\rho^{NA}(\mathbf{r}) - \frac{1}{2}\int d\mathbf{r} V_{\delta H}[\rho(\mathbf{r}) - \rho^{NA}(\mathbf{r})] \tag{2.22}$$

and the short-ranged (SR) ionic interaction energy E_{SR}:

$$\begin{aligned}
E_{SR} &\equiv \sum_I E^I_{SR} + \frac{1}{2}\sum_{i\neq j} V_{SR}(|\mathbf{R}_I - \mathbf{R}_J|), \\
E^I_{SR} &= \frac{1}{2}\int\int d\mathbf{r} d\mathbf{r}' \frac{\rho^{NA,K}(\mathbf{r})\rho^{NA,K}(\mathbf{r}')}{|\mathbf{r}-\mathbf{r}'|}, \\
V_{SR}(|\mathbf{R}_I - \mathbf{R}_J|) &= \frac{Z_I Z_J}{|\mathbf{R}_I - \mathbf{R}_J|} - \int\int d\mathbf{r} d\mathbf{r}' \frac{\rho^{NA,K}(\mathbf{r}-\mathbf{R}_I)\rho^{NA,J}(\mathbf{r}-\mathbf{R}_J)}{|\mathbf{r}-\mathbf{r}'|}.
\end{aligned}$$

2.3.2 Comments on Density Functional Methods

The great advantage of the HK theorem and KS equations is that they reduce the fully interacting N-particle problem to solving a set of self-consistent single-particle equations. In principle, the fully interacting N-particle problem can be solved exactly given the energy functional $E[\rho]$. Unfortunately, the exact form is unknown. However, with the use of a minimal number of well-controlled approximations, it is found that density functional theory is surprisingly accurate and has been successfully applied to a wide range of systems.

Several reasons for this surprising success have been proposed[40]. It can be shown that the exchange-correlation energy can be written in terms of a mean-field interaction with an exchange-correlation hole ρ_{XC} [64]:

$$E_{XC} = \frac{1}{2}\int d\mathbf{r}d\mathbf{r}' \frac{\rho_{XC}(\mathbf{r},\mathbf{r}-\mathbf{r}')\rho(\mathbf{r}')}{|\mathbf{r}-\mathbf{r}'|}. \tag{2.23}$$

In particular, E_{XC} depends only on the spherical average of $\frac{1}{|\mathbf{r}-\mathbf{r}'|}$, weighted with the exchange correlation hole ρ_{XC}. Thus, it can be expected that the exchange-correlation energy depends only weakly on the details of ρ_{XC} [40].

The Kohn-Sham eigenvalues $\{E^i\}$ were introduced as Lagrange multipliers in Eq. 2.13. Their physical meaning is not clear, but it is standard practice in condensed matter physics to assume they represent real quasi-particle eigenvalues. It has been found that the eigenvalues near the Fermi energy are reasonably close to the real excitation energies[40]. In any case, there is no simple alternative and we will proceed to interpret the eigenvalues and eigenstates as those of real quasi-particles.

2.4 Energy Functionals

The central challenge of DFT is to determine the energy functional $E[\rho]$. Little is known about the exact form of $E[\rho]$, but several well-controlled approximations, based upon analyses of the homogeneous electron gas of density $\rho(\mathbf{r}) = \rho_0$, have been used with varying degrees of success.

2.4.1 Thomas-Fermi Theory

The earliest density functional theory, Thomas-Fermi (TF) theory [64], was developed before the HK theorem was proven. The TF total energy functional is derived from a homogeneous non-interacting electron gas:

$$E_{TF}[\rho] = \frac{3(3\pi^2)^{2/3}}{10}\int d\mathbf{r}\rho^{5/3}(\mathbf{r}) + \frac{1}{2}\int d\mathbf{r}d\mathbf{r}'\frac{\rho(\mathbf{r})\rho(\mathbf{r}')}{|\mathbf{r}-\mathbf{r}'|} + \int d\mathbf{r}\rho(\mathbf{r})V(\mathbf{r}). \tag{2.24}$$

Thomas-Fermi-Dirac (TFD) theory[64] adds a correction due to exchange effects

$$E_{TFD}[\rho] = \frac{3(3\pi^2)^{2/3}}{10}\int d\mathbf{r}\rho^{5/3} + \frac{1}{2}\int d\mathbf{r}d\mathbf{r}'\frac{\rho(\mathbf{r})\rho(\mathbf{r}')}{|\mathbf{r}-\mathbf{r}'|} - \frac{3}{4}\left(\frac{3}{\pi}\right)^{1/3}\int d\mathbf{r}\rho^{1/3} + \int d\mathbf{r}\rho(\mathbf{r})V(\mathbf{r}). \tag{2.25}$$

These functionals have well known problems. For example, it can be shown that no bonding of molecules is predicted within Thomas-Fermi theory[64].

2.4.2 Local Density Approximation

The local density approximation (LDA) is often used in solutions of the Kohn-Sham equations.[1] When solving the KS equations, only the non-classical corrections $E_{XC}[\rho] = T[\rho] - T_{KS}[\rho] + E_x[\rho] + E_c[\rho]$ must be approximated. These are, presumably, small corrections to the Kohn-Sham non-interacting energy and can be calculated accurately for the high and low-density limits of the homogeneous electron gas[15] and interpolated as a function of ρ_0. The result, interpolated for numerical covenience, is given by the rational polynomial[29].

---

[1] While the Thomas-Fermi approximation is a local density approximation also, the term LDA is normally used when local approximations are made for E_{XC}, as in Kohn-Sham theory, and not the total energy E_{tot}, as in TF theory.

Within LDA, the energy of an inhomogeneous electron gas is calculated using the following local approximation:

$$\begin{aligned} E_{XC}[\rho(\mathbf{r})] &= \int d\mathbf{r}\rho(\mathbf{r})\varepsilon_{XC}^{\rho_0}(\rho(\mathbf{r})), \\ \varepsilon_{XC}^{\rho_0} &\equiv \frac{E_{XC}(\rho_0)}{\rho_0}. \end{aligned}$$

2.4.3 Beyond the Local Density Approximation

A natural way to extend the LDA is to include information about inhomogeneities. The magnitude of the local gradient $|\nabla\rho(\mathbf{r})|$ is a measure of the inhomogeneity and can be included in the exchange-correlation functional: $E_{XC}(\mathbf{r}) = E_{XC}(\rho(\mathbf{r}), |\nabla\rho(\mathbf{r})|)$. Early attempts suggested that a naive expansion in orders of $|\nabla\rho(\mathbf{r})|$ was less accurate than the original LDA[65]. This can be understood in terms of exact sum rules and constraints on E_{XC} derived form the exchange-correlation hole[65]. It turns out that naive gradient expansions violated some of these constraints while the LDA does not. The interpretation is that LDA corresponds to an approximate, but physical system, while the gradient expansions correspond to unphysical systems. The Generalized Gradient Approximation (GGA) was introduced by explicitly constructing a functional that met many of the known constraints imposed on ρ_{XC}[65]. This illustrated the importance of sum rules and constraints in DFT and demonstrated that increasingly accurate functionals may be constructed by deriving more stringent constraints and constructing functionals that satisfy them.

2.5 Pseudopotential Approximation

Once the exchange-correlation functional has been chosen, the system is defined up to an external potential $V_{ext}(\mathbf{r})$. In *ab-initio* analyses, one important component of the external potential is generated by the nuclear cores $\{\mathbf{R}_K\}$, as in Eq. 2.1. These potentials are singular near the cores and some care must be taken when solving the Kohn-Sham equations, particularly when using a real-space basis.

When atoms come together to form a solid, the core electrons, localized around each atom, will only interact weakly with the core electrons of other atoms. In the pseudopotential approximation, the core electrons are assumed to be frozen. As such, they act much like the nuclear core in generating an external potential. The total external potential of the original reference or *all-electron* (AE) atom, including the nuclear core and the core electrons, is then replaced by a smooth, non-singular potential known as the pseudopotential (PS) which only acts on the valence electrons. The pseudopotential can be constructed to satisfy a number of transferability conditions so that it may be used in a variety of different chemical environments.

When the core electrons are removed, a large part of the total energy is ignored, thus only changes in the total energy due to rearrangement of the valence charege have meaning in pseudopotential calculations. This is acceptable so long as the atomic cores interact weakly with neighbouring atoms and are not sensitive to their environment.

Because the core states have been effectively removed from the problem, the eigenstates of the pseudopotential, or pseudoorbitals, need not be orthogonal to the core electrons and are therefore nodeless in the core region, $r < r_c$. As a result, the pseudoorbitals are generally smoother and easier to represent on a numerical grid than the orbitals of the original all-electron atom. Outside the core region, $r > r_c$, the pseudopotential and the pseudoorbitals are identical to the corresponding all-electron potential and orbitals.

Empirical pseudopotentials are based on fits to bulk properties of a system and, not surprisingly, agree well with expermental results for bulk systems. However, these potentials are not very transferable, meaning that they may not work when used to model systems with chemical environments different from the bulk. The development of *ab-initio*, norm-conserving, pseudopotentials by Hamman, Schlüter and Chiang (HSC)[32, 7] allows for a systematic construction of transferable pseudopotentials.

The HSC pseudopotential is referred to as an *ab-initio* pseudopotential because it is derived from an *ab-initio* density functional calculation of the properties of a single reference atom. The first step is to solve the Kohn-Sham problem for an all-electron atom, including core states and valence states. This yields the all-electron wave functions $\{\psi^{AE}\}$ and the all-electron potential $V^{AE}(\mathbf{r})$. The pseudopotential V^{PS} is designed to satisfy the following constraints:

1. The all-electron eigenvalues are equal to the pseudopotential eigenvalues:
$$E^{AE} = E^{PS}. \tag{2.26}$$
2. The potential outside a cutoff radius r_c is identical to the all-electron potential:
$$V^{PS}(r > r_c) = V^{AE}(r > r_c). \tag{2.27}$$
3. The pseudoorbitals (eigenstates of the pseudopotential) are identical to the all electron eigenstates outside the cutoff radius r_c:
$$\psi^{PS}(r > r_c) = \psi^{AE}(r > r_c). \tag{2.28}$$

4. The charge inside r_c is the same for the pseudopotential and all-electron potential:

$$\int_0^{r_c} drr^2 \, \psi^{PS}(r)^{2} = \int_0^{r_c} drr^2 \, \psi^{AE}(r)^{2}. \tag{2.29}$$

The first constraint ensures that the pseudoatom and the all-electron atom have the same spectra at the valence energies. The second constraint ensures that the potential outside the core region is not changed by the pseudopotential approximation. The third and fourth constraints ensure that the logarithmic derivatives of the all-electron atom and the pseudoatom agree to first order outside the cutoff radius r_c. Since the logarithmic derivative is related to the phase shift of a free electron scattering off a radial potential, this ensures that the scattering properties of the pseudoatom match those of the all-electron atom. When the pseudoatom is placed in a different chemical environment , the levels will shift due to bonds or interactions with other atoms. In order for a pseudopotential to be transferable, the pseudopotential must mimic the all-electron atoms for a wide range of energies and not just at the eigenenergies. In fact, numerical calculations show that the scattering properties of the all-electron potential and the pseudopotential are identical over a wide range of energies[32].

The accuracy of the HSC pseudopotential is controlled by the cutoff radius r_c. In general, the smaller the cutoff-radius, the more transferable the pseudopotential. However, as the cutoff-radius is decreased, the pseudopotential becomes “harder” in the sense that a finer grid and more plane waves are necessary to represent the pseudopotential accurately. This is of particular concern in plane-wave approaches to solving the KS equations[52]. In this work, the pseudopotential matrix elements are pre-tabulated and can be calculated on a fine grid and we are not concerned with optimizing the softness of the pseudopotential.

A limitation of the HSC pseudopotential is that it represents a linearization of the exchange-correlation potential:

$$V_{XC}^{PS}(r) = V_{XC}(\rho^{valence}). \tag{2.30}$$

This may be corrected using a non-linear core correction when calculating the exchange-correlation potential[8].

The construction introduced by HSC to satisfy the above constraints is not unique and other norm-conserving pseudopotentials may be constructed but the HSC pseudopotential is by far the most popular.

2.5.1 Non-Local Pseudopotentials

In order to ensure that the phase shift of the pseudopotential is correct for all angular momentum eigenstates l, one must in general use a non-local pseudopotential that is angular momentum dependent:

$$V_{NL} = \sum_{l} |l\rangle V_l \langle l|. \tag{2.31}$$

The semi-local HSC pseudopotential involves a projection over the solid angle $\Omega_{\mathbf{r}'}$:

$$V_{HSC}(\mathbf{r},\mathbf{r}') = \sum_{lm} |Y_{lm}(\Omega_{\mathbf{r}})\rangle V_l(\mathbf{r})\delta(r-r')\langle Y_{lm}(\Omega_{\mathbf{r}'})|. \tag{2.32}$$

An alternative construction, due to Kleinman and Bylander (KB) [46], introduces a separable form in which the projection is over both the radial and angular component:

$$V_{KB}(\mathbf{r},\mathbf{r}') = \sum_{lm} |Y_{lm}(\Omega_{\mathbf{r}})W_l(r)\rangle \varepsilon_l \langle W_l(r')Y_{lm}(\Omega_{\mathbf{r}'})| W_l(r) \equiv V_l(r)\psi_l(r)\varepsilon \equiv \frac{\langle \psi_l | V_l(r) | \psi_l \rangle}{\langle \psi_l | V_l^2(r) | \psi_l \rangle}. \tag{2.33}$$

The projection in Eq. 2.33 is generally easier to calculate than the projection over solid angle in Eq. 2.32. However, the Kleinman-Bylander transformation can lead to unphysical ghost states [30] in which the lowest p state is lower than the lowest s There exist, in the literature, lists of Kleinman-Bylander potentials that have been checked for ghost states.

2.6 Basis Sets

Given the appropriate exchange-correlation potential and pseudopotential, the Kohn-Sham Hamiltonian, Eq. 2.13, is well defined except for boundary conditions on the Hartree potential and explicit external potentials $V_{ext}(\mathbf{r})$. To solve the Kohn-Sham equations numerically, one must employ a set of basis functions in order to efficiently represent the electronic wave functions. Several factors determine the choice of basis including ease of implementation, speed, accuracy, and geometry of the system. In general, one chooses between a plane-wave basis, localized in **k**-space, or a basis that is localized in real space.

2.6.1 Plane-Wave Calculations

Plane wave methods are very accurate and relatively simple to implement compared to real space techniques. The starting point for a plane-wave calculation is an expansion of the wave functions in terms of a sum of plane waves:

$$\psi^i = \sum_{\mathbf{k}} c^i_{\mathbf{k}} e^{-i\mathbf{k}\cdot\mathbf{r}}. \tag{2.34}$$

Such expansions are ideal for studying systems with periodic boundary conditions because only the reciprocal lattice vectors $\{\mathbf{G}\}$ need to be included in the expansion in terms of basis functions [4]. In practice, a finite set of $\{\mathbf{k}\}$ is chosen sufficient so that the wave function can be expressed accurately. This accuracy can also be increased in a controlled fashion by restricting the wave vectors such that their magnitude is less than a specified cutoff $|\mathbf{k}| < k_{cutoff}$, in order to capture oscillations on the scale of $\nabla r \approx \frac{\pi}{k_{cutoff}}$. The resolution and accuracy of the expansion can be systematically increased by increasing k_{cutoff}. For these reasons, plane wave based calculations are common in condensed matter physics. An excellent review is given by Payne et al [52].

The number of plane waves is generally much larger than the number of electrons: $N_{basis} \gg N_{el}$. In the literature, there exist well-known preconditioners and efficient iterative techniques to solve the KS equations for such large basis sets [52].

2.6.2 Bloch's Theorem

Bloch's theorem states that in a periodic solid each electronic wave function can be written as the product of a cell-periodic part and a wave-like part [4],

$$\Psi_i(\mathbf{r}) = e^{i\mathbf{k}\cdot\mathbf{r}} f_i(\mathbf{r}). \tag{2.35}$$

The cell-periodic part of the wave function can be expanded using a basis set consisting of a discrete set of plane waves whose wave vectors are reciprocal lattice vectors of the crystal,

$$f_i(\mathbf{r}) = \sum_{\mathbf{G}} c_{i,\mathbf{G}} e^{i\mathbf{G}\cdot\mathbf{r}}, \tag{2.36}$$

where the reciprocal lattice vectors $\mathbf{G}$ are defined by $\mathbf{G}\cdot\mathbf{l} = 2\pi m$ for all $\mathbf{l}$ where $\mathbf{l}$ is a lattice vector of the crystal and m is an integer. Therefore each electronic wave function can be written as a sum of plane waves,

$$\Psi_i(\mathbf{r}) = \sum_{\mathbf{G}} c_{i,\mathbf{k}+\mathbf{G}} e^{i(\mathbf{k}+\mathbf{G})\cdot\mathbf{r}}. \tag{2.37}$$

2.6.3 Plane-Wave Representation of Kohn-Sham Equations

When plane waves are used as a basis set for the electronic wave functions, the Kohn-Sham equations get a particularly simple form. Substitution of Eq. 2.37 into 2.13

$$\sum_{\mathbf{G}'} \left[(\frac{1}{2}|\mathbf{k}+\mathbf{G}|^2 \delta_{\mathbf{G}\mathbf{G}'} + V_{ion}(\mathbf{G}-\mathbf{G}') + V_H(\mathbf{G}-\mathbf{G}') + V_{XC}(\mathbf{G}-\mathbf{G}') \right] \Bigg(c_{i,\mathbf{k}+\mathbf{G}'} = \varepsilon_i c_{i,\mathbf{k}+\mathbf{G}}. \tag{2.38}$$

In this form, the kinetic energy is diagonal, and the various potentials are described in terms of their Fourier transforms.

2.7 Solution of the Kohn-Sham Equations

The single-particle Hamiltonian that appears in the Kohn-Sham equations depends on its solutions $\{\psi_i\}$ through the density: $H = H[\rho(\mathbf{r})]$. Thus, it is a non-linear eigenvalue equation which must be solved self-consistently. This self-consistent iteration starts with an initial guess for the density matrix. Given an input density matrix, the KS Hamiltonian may be constructed. From the KS Hamiltonian, an output density matrix is calculated and compared to the input density matrix. If the two density matrices do not match, a new input density is formed based on the output density matrix. This process is repeated until self-consistency is achieved at which point the iteration stops, data analysis is performed and physical quantities are calculated form the electronic ground state. Then, the external variables, such as the nuclear positions $\{\mathbf{R}_K\}$ are updated and a new self-consistent calculation is performed. Each step is briefly outlined below.

2.7.1 Initialize Density

The first step in solving the KS equations is to choose an initial trial density $\rho^0(\mathbf{r})$. A natural choice is a superposition of neutral atom densities: $\rho^0(\mathbf{r}) = \sum_I \rho^{NA}(\mathbf{r} - \mathbf{R}_I)$. On the other hand, a reasonable guess at the self-consistent density based on a previous solution of the KS equations may be available. For example, in a molecular dynamics simulation or another simulation that evolves incrementally from time t to time $t+1$, the self-consistent density at time t can be used as an input to the self-consistent iteration at time $t+1$. The method described in this work is not sensitive to the initial choice of density ρ^0 but other methods, such as the iterative solution method used in plane wave calculations, may not converge to the correct result if the initial density is not chosen properly [52]. Some methods are known to diverge for inappropriate choices of initial density [11, 61].

2.7.2 Constructing the Hamiltonian

The Hamiltonian matrix $H = A[\rho]$ depends on $\rho(\mathbf{r})$ through the effective potential $V^{eff}[\rho(\mathbf{r})]$:

$$V^{eff}(\mathbf{r}) = V_H[\rho(\mathbf{r})] + V_{XC}(\rho(\mathbf{r})). \tag{2.39}$$

The Hartree potential, Eq 2.18, is obtained by solving the Poisson equation with suitable boundary conditions on the surface S:

$$\nabla^2 V_H = 4\pi\rho(\mathbf{r}) V_H|_S = V_S. \tag{2.40}$$

The choice of boundary conditions may depend on the method used to solve the Poisson equation. For example, a Fourier transform solution to the Poisson equation,

$$V_H(\mathbf{k}) = \frac{4\pi\rho(\mathbf{k})}{|\mathbf{k}|^2} \tag{2.41}$$

introduces an implicit periodic boundary condition. Of course, for bulk systems, this choice is appropriate. For molecules, the choice is less clear. Provided the simulation box is large enough so that the molecule does not interact with its images, the above Fourier transform method may be used to determine V_H. Alternatively, the Poisson equation may be solved in real space. In this case, appropriate boundary conditions must be chosen for V_H. For example, if the simulation box is large enough, homogeneous boundary conditions may be assumed

$$V_H|_S = 0 \tag{2.42}$$

or a multipole expansion may be performed [38]. Given the effective potential $V^{eff}(\mathbf{r})$, the matrix elements must be calculated in the chosen basis set. This is a well-defined procedure and, depending on the basis set, may be more or less complicated.

CHAPTER III

QUANTUM TREATMENT OF HYDROGEN

3.1 Why Do We Need a New Program?

There are many software packages such as VASP, ABINIT, SIESTA that performs *ab intio* calculations based on DFT. These programs, however, treat only electrons quantum mechanically but nuclei classically. In most cases, it is an acceptable approximation due to large mass of nuclei compared to electron mass. Quantum treatment of nuclei gives small improvement in energies, but no qualitatively different results. Usually the improvement is insignificant and thus it is not worth the efforts.

As our results demonstrate, however, a special circumstance arises for H atoms in the vicinity of vacancy defects on metal surfaces. Surface metal atoms and neighboring H atoms form a potential well that traps H atoms and enhances the quantum effect on their wave functions. The correct geometry of vacancy defects on metal surfaces cannot be obtained without full consideration of quantum effect on H atoms. None of the readily available software packages go beyond the classical treatment of nuclei.

We developed our new software package APPSES for this particular purpose in mind. This program solves the Schrödinger's equation for a single particle in arbitrary potential with periodic boundary conditions.

To use this code effectively, we need to construct potential energy surface for a nucleus very carefully based on rigorous *ab initio* methods. For a single particle, as the H atom in two-vacancy defect on a Pd(111) surface, the potential is 3-dimensional. The potential energy surface (PES) is explored and mapped out by calculating the adsorption energy E_a of the H atom under consideration. Each point of the potential energy surface requires a full DFT calculation with large unit cell and hundreds of atoms and several times more electrons.

3.2 Bloch Theorem

F. Bloch proved that the solutions of the Schrödinger equation for a periodic potential must be of a special form[4]:

$$\Psi_{\mathbf{k}}(\mathbf{r}) = u_{\mathbf{k}}(\mathbf{r}) e^{i\mathbf{k}\cdot\mathbf{r}}, \tag{3.1}$$

where $u_{\mathbf{k}}(\mathbf{r})$ has the period of the crystal lattice with $u_{\mathbf{k}}(\mathbf{r}) = u_{\mathbf{k}}(\mathbf{r}+\mathbf{T})$. The result expresses the Bloch theorem:

> The eigenfunctions of the wave equation for a periodic potential are the product of a plane wave $e^{i\mathbf{k}\cdot\mathbf{r}}$ times a function $u_{\mathbf{k}}(\mathbf{r})$ with the periodicity of the crystal lattice.

3.3 Schrödinger Equation for a Particle in a Periodic Potential

We need to solve the Schrödinger equation

$$H\Psi = \left(-\frac{\hbar^2}{2m}\nabla^2 + U(\mathbf{r})\right)\Psi = \varepsilon\Psi \tag{3.2}$$

when the potential is periodic in space.

Let $U(\mathbf{r})$ denote the potential energy of a particle in a lattice of lattice translation vector $\mathbf{T}$. We know that the potential energy is invariant under a crystall lattice translation: $U(\mathbf{r}) = U(\mathbf{r}+\mathbf{T})$. A function invariant under a crystall lattice translation may be expanded as a Fourier series in the reciprocal lattice vector $\mathbf{G}$. We write the Fourier series for the potential energy as

$$U(\mathbf{r}) = \sum_{\mathbf{G}} U_{\mathbf{G}} e^{i\mathbf{G}\cdot\mathbf{r}}. \tag{3.3}$$

The values of the coefficients $U_{\mathbf{G}}$ for actual crystal potentials tend to decrease rapidly with increasing magnitude of $\mathbf{G}$. For a bare coulomb potential $U_{\mathbf{G}}$ decreases as $1/G^2$.

The wave function $\Psi(\mathbf{r})$ may be expressed as a Fourier series summed over all values of the wavevector permitted by the boundary conditions, so that

$$\Psi = \sum_{\mathbf{q}} C_{\mathbf{q}} e^{i\mathbf{q}\cdot\mathbf{r}} \tag{3.4}$$

We now place the expansions Eq. 3.3 and Eq. 3.4 into Schrödinger equation Eq. 3.2. The kinetic energy term gives

$$\frac{p^2}{2m}\Psi = -\frac{\hbar^2}{2m}\nabla^2\Psi = \sum_{\mathbf{q}} \frac{\hbar^2}{2m} q^2 C_{\mathbf{q}} e^{i\mathbf{q}\cdot\mathbf{r}}. \tag{3.5}$$

The term in the potential energy can be written

$$U\Psi = \sum_{\mathbf{G}} U_{\mathbf{G}} e^{i\mathbf{G}\cdot\mathbf{r}} \Big) \sum_{\mathbf{q}} C_{\mathbf{q}} e^{i\mathbf{q}\cdot\mathbf{r}} \Big)\Big(\tag{3.6}$$

$$= \sum_{\mathbf{G}\mathbf{q}} U_{\mathbf{G}} C_{\mathbf{q}} e^{i(\mathbf{G}+\mathbf{q})\cdot\mathbf{r}} = \sum_{\mathbf{G}\mathbf{q}'} U_{\mathbf{G}} C_{\mathbf{q}'-\mathbf{G}} e^{i\mathbf{q}'\cdot\mathbf{r}}. \tag{3.7}$$

We change the names of the summation indices from $\mathbf{G}$ and $\mathbf{q}'$, to $\mathbf{G}'$ and $\mathbf{q}$ so that the Schrödinger equation becomes

$$\sum_{\mathbf{q}} e^{i\mathbf{q}\cdot\mathbf{r}} \left\{ \left(\frac{\hbar^2}{2m}q^2 - \varepsilon\right) C_{\mathbf{q}} + \sum_{\mathbf{G}'} U_{\mathbf{G}'} C_{\mathbf{q}-\mathbf{G}'} \right\} = 0. \tag{3.8}$$

Since the plane waves satisfying the boundary condition are an orthogonal set, the coefficient of each separate term in Eq. 3.8 must vanish, and therefore for all allowed wave vector $\mathbf{q}$,

$$\left(\frac{\hbar^2}{2m}q^2 - \varepsilon\right) C_{\mathbf{q}} + \sum_{\mathbf{G}'} U_{\mathbf{G}'} C_{\mathbf{q}-\mathbf{G}'} = 0. \tag{3.9}$$

It is convenient to write $\mathbf{q}$ in the form $\mathbf{q} = \mathbf{k} - \mathbf{G}$, where $\mathbf{G}$ is a reciprocal lattice vector chosen so that $\mathbf{k}$ lies in the first Brillouin zone. The equation above becomes

$$\left(\frac{\hbar^2}{2m}(\mathbf{k}-\mathbf{G})^2 - \varepsilon\right) C_{\mathbf{q}} + \sum_{\mathbf{G}'} U_{\mathbf{G}'} C_{\mathbf{k}-\mathbf{G}-\mathbf{G}'} = 0. \tag{3.10}$$

or, if we make the change of variables $\mathbf{G}' \to \mathbf{G}' - \mathbf{G}$,

$$\left(\frac{\hbar^2}{2m}(\mathbf{k}-\mathbf{G})^2 - \varepsilon\right) C_{\mathbf{k}-\mathbf{G}} + \sum_{\mathbf{G}'} U_{\mathbf{G}'-\mathbf{G}} C_{\mathbf{k}+\mathbf{G}'} = 0 \tag{3.11}$$

If we make the change of variables $\mathbf{G}' \to -\mathbf{G}'$ and $\mathbf{G} \to -\mathbf{G}$

$$\left(\frac{\hbar^2}{2m}(\mathbf{k}+\mathbf{G})^2 - \varepsilon\right) C_{\mathbf{k}+\mathbf{G}} + \sum_{\mathbf{G}'} U_{\mathbf{G}-\mathbf{G}'} C_{\mathbf{k}+\mathbf{G}'} = 0 \tag{3.12}$$

This equation are nothing but restatements of the Schrödinger equation in momentum space, simplified by the fact that because of the perriodicity of the potential, $U_{\mathbf{k}}$ is nonvanishing only when $\mathbf{k}$ is a vector of the reciprocal lattice.

CHAPTER IV

FIRST PRINCIPLE STUDY OF METAL SURFACES

4.1 Introduction

The dissociative adsorption of the diatomic molecule H_2 is a central step in many industrially important catalytic processes specially in the fuel cell technology. The interaction of hydrogen with transition-metal surfaces has been extensively investigated in recent years[68, 2, 69, 27, 72, 66, 79, 59, 81, 34, 42, 63, 53, 43]. First-principles calculations at a high coverage have found that hydrogen adsorbs in the threefold hollow fcc site on Pt(111)[63], Ni(111)[69, 53] and Pd(111)[59, 81, 34] surfaces. Hydrogen is also found to diffuse easily with relatively small energy barriers via the activated tunneling mechanism rather than classical hopping[68, 43, 53].

Despite these extensive investigations, the exact nature of vacancy defects of H atoms on metal surfaces was not fully understood to date. Recently, from the scanning tunneling microscopy (STM) experiment, Mitsui *et al* reported the discovery of new and somewhat unexpected facts about hydrogen adsorption on palladium[76, 77]. Their observation raised two main questions that have not yet been answered satisfactorily. (1) A two-vacancy defect appears as a bright triangle occupying three nearest-neighbor fcc sites in the observed STM image. In their original dissertation, the authors gave a simple explanation interpreting the image as the time average of a single H atom moving around rapidly via thermally activated diffusion among three fcc sites connected by a central hcp site. Although, this model of classical hoping of hot H atom can explain the STM image of a two-vacancy defect, it quickly runs into difficulty in explaining similar images for larger vacancy defects. As analyzed later in Sec. 4.3.3 in details, this classical motion of H atoms requires an extraordinary coordination among H atoms moving around—fast enough to blur the image of the entire region—inside vacancy defects. Consequently, the motion of H atoms becomes severely restricted as the number of H atoms need to move around increases. (2) Mitsui *et al* also reported that two-vacancy sites are virtually inactive and aggregates of three or more hydrogen vacancies are required for efficient H_2 dissociation. This is totally contrary to the conventional Langumir principle that two active sites in close proximity should be sufficient to facilitate the dissociation of a H_2 molecule containing two H atoms. Lopez and co-workers proposed one explanation using chemical poisoning of Pd around the active sites by calculating activation energies associated with reaction paths[57]. This calculation, however, is based on the geometry of two- and three-vacancy defects that contains exactly two and three empty fcc sites. As our results indicate, these are not correct structures for two- and three-vacancy defects. Each of these configuration is only one of many possible configurations that are changing rapidly. Furthermore, a three-vacancy defect, for example, involves the triangular area covering six fcc sites.

Understanding the precise ground state geometry of two- and three-vacancy defect aggregates is therefore one of the most crucial steps in understanding these intriguing observations. The process of dissociative adsorption cannot be understood or even be calculated without the correct structures to start with. Furthermore, due to its small mass, hydrogen atom is known to exhibit considerable quantum effects on metal surfaces. Källén and *et al* treated 1/4 monolayer of hydrogen atoms adsorbed on a Pt(111) surface quantum mechanically and found its wave function to be delocalized around the hollow fcc sites where potential energy is minimum[31]. Puska and *et al* interpreted vibrational excitations from the delocalization of chemisorbed hydrogen atom on Ni(100) surface[53]. As our results show, the vacancy defects on Pd(111) create a special circumstance that requires quantum treatment of H atoms in vacancy defects.

In this letter we address all of these issues by treating the motion of a hydrogen atom in the vicinity of vacancy defects quantum-mechanically. The potential for the quantum mechanical calculations is mapped out by careful first-principles electronic structure calculations. We find the quantum effects to be critical in changing the hollow hcp sites to be energetically more favorable than hollow fcc sites. Consequently, hydrogen atoms in the vicinity of vacancy defects become delocalized and concentrate more in the hcp sites to lower the kinetic energy by maximizing their symmetry and thus lower the total energy. We then demonstrate that the same quantum effect elegantly explains the STM images of vacancy defects without resorting to classical thermal diffusion of hydrogen atoms. More importantly, our ground state geometry of vacancy defects also provides a compelling argument for the efficacy of three-vacancy defects and inertness of two-vacancy defects in adsorbing H_2 molecules.

4.2 Methods and Computational Details

4.2.1 Methods

The static potential energy surface in the vicinity of vacancy defects is mapped out by the electronic structure calculations based on the first principles density-functional theory [24, 62, 48]. The interaction between valence electrons and positive ions shielded by core electrons are represented by ultra-soft pseudo-potentials[16, 26]. The wave function of electrons are expanded in terms of plane-wave basis set and all plane waves that have kinetic energy less than 250 eV are included in expanding the wave functions. Exchange correlation effects were treated within the local-density approximation (LDA) based on the quantum Monte Carlo simulations of Ceperly and Alder[15] as parametrized by Perdew and Zunger[36]. For the determination of the self-consistent electron density $6{\times}6{\times}1$ Monkhorst-Pack k-point set has been used. The structure optimizations were performed until the energy difference between successive steps becomes less than 10^{-3} eV.

4.2.2 Bulk

The bulk calculations were performed to obtain the optimized lattice constant for Pd crystall in FCC structure. The convergence of the total energy was carefully monitored to ensure that the energy cut-off and the *k* point sampling we had chosen were adequate. The equilibrium lattice constant we obtained from this bulk calculation was 3.86 Å. Considering the fact that LDA calculations consistently predict smaller values within 1% of experimentally measured lattice constants, our result is in an excellent agreement with the experimental value of 3.89 Å[12].

4.2.3 Slab

Once the equilibrium lattice constant is determined, we construct a slab supercell representing the unreconstructed (111) surface. This was done by periodically replicating the unit cell with optimum lattice constant obtained in the bulk calculation. As shown in Fig. 4.1, we separated adjacent slabs by a vacuum region of 12 Å, which we confirmed was more than sufficient to make the interaction between neighboring slabs negligible.

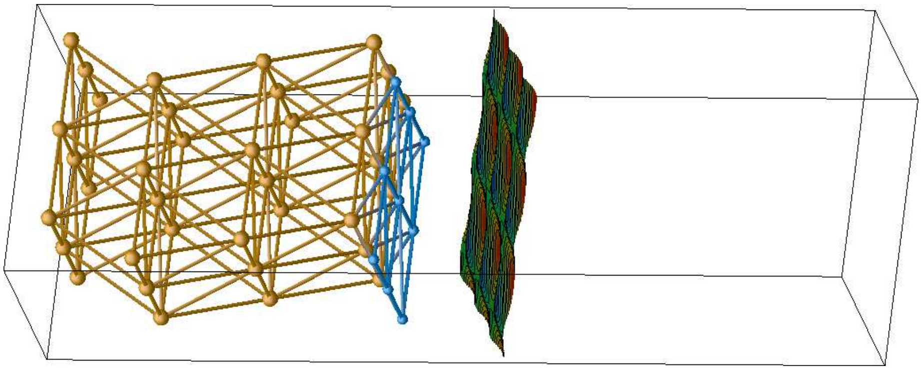

Figure 4.1 The 3×3 surface unit-cell used in this dissertation. The slab of Pd has 4 layers. The hydrogen layer is located just above the top Pd layer which has 9 Pd atoms and 9 fcc sites. These hydrogen atoms are absorbed in fcc site on Pd surface. The vacuum region is 12 Å. The simulated STM image shown over the hydrogen layer.

To ensure that we have adequate number of layers in the Pd slab we calculated the adsorption energy of H as a function of the number of Pd layers. Our results are summarized in Table 4.1. During the calculations we keep the Pd atoms fix at the positions of a relaxed clean Pd(111) surface. The Pd atoms in the first layer in the bottom are held in place during structure optimization to simulate the bulk substrate layers. The adsorption energy is computed through[59]

$$E_{\mathrm{a}} = E_{\mathrm{form}}(\mathrm{Pd}+\mathrm{H}) - E_{\mathrm{form}}(\mathrm{Pd}) - \frac{1}{2}E_{\mathrm{bind}}(\mathrm{H_2}), \tag{4.1}$$

where E_{form} is the formation energy of the hydrogen covered and bare Pd slabs. We obtained the formation energy for H_2 molecule to be -4.54 eV, which is comparable to experimental value of -4.75 eV[49] and also compares well with previously reported calculated values[66].

Table 4.1 Results for the test of number of Pd atom layers in the slab geometry. $\Delta E_a(\mathrm{H_2})$ is obtained from the adsorption energy of H_2 into a $3V_H$vacancy defect. All values are given in eV.

	E_a(H)	$\Delta E_a(\mathrm{H_2})$
3 layers of Pd	-4.28	1.71
4 layers of Pd	-4.31	1.83
5 layers of Pd	-4.28	1.74
6 layers of Pd	-4.28	1.84

We found that the adsorption energies for the top, hcp, fcc, and bridge sites are well converged at four layers, confirming that the thickness of the slab in our calculations was sufficient to reduce the interaction between the atoms in the images of the slab due to periodic boundary conditions we employed to a negligible level. Our results compares well with previous calculations with similar number of layers[59, 34]. Our results are also consistent with several experimental observations[9, 44, 47, 75].

4.2.4 Vacancy Defect Configurations

Fig. 4.2 shows the hydrogen vacancy configurations on Pd(111) surface considered in the present study. Pd atoms are represented by larger white circles and H atoms are represented by small black circles. The smaller white circles represent empty fcc sites. The quantum mechanically delocalized H atoms are represented by magenta (color) or gray (black and white) circles. Fig. 4.2(a) shows a fully hydrogenated Pd(111) surface. In this configuration, labeled as 0V, all fcc sites on Pd(111) surface are occupied by H atoms. No hcp site is occupied. Fig. 4.2(b) shows a single hydrogen atom vacancy defect (1V). Fig. 4.2(c) and Fig. 4.2(d) show the conventional models for two- and three-vacancy hydrogen defects. They are labeled as 2V and $3V_H$. The subscript “H” indicates that the trimer contains an hcp site in the middle. However, as we demonstrate later in this dissertation, these are not ground-state configurations when full quantum mechanical treatment is given to hydrogen atom motion. A two-vacancy defect in ground-state ($2V_Q$) is shown in Fig. 4.2(e) where one delocalized hydrogen atom occupies the central hcp site leaving three fcc sites unoccupied. The subscript “Q” indicates its quantum mechanical origin. Fig. 4.2(f) shows a three-vacancy hydrogen defect ($3V_Q$) in the ground-state. It contains three delocalized hydrogen atoms concentrated on three hcp sites while leaving six fcc sites unoccupied.

The first step in addressing many intriguing observations associated with multi-vacancy defects is to understand the simplest non-trivial vacancy defects. In our case, that would be a two-vacancy defect. As we show later, the quantum effects manifested in the structure of two-vacancy defect enables us to elucidate many puzzling observations with simple reasonings. Therefore, in this dissertation we focus mainly on the determination of the ground-state configuration of a two-vacancy defect.

4.2.5 Static Potential Energy Surface

To determine a minimum energy structure of a two-vacancy defect quantum mechanically, we need to construct potential energy surface for hydrogen atoms. Since each point in this multi-dimensional vector space requires a full DFT calculation with the slab supercell we constructed, it is impractical to treat many hydrogen atoms. Fig. 4.3 and Fig. 4.4 are the plots of the potential energy surface (3-dimensional in this case) in the vicinity of $3V_H$ defect. From these plots, we can easily conclude that any pathway for hydrogen atom other than from *unoccupied* fcc site to *unoccupied* hcp site requires overcoming large potential barriers. It also should be clear from Fig. 4.2(e) that there is no low energy barrier pathway for neighboring H atoms to move into the defect region. Therefore, we can con-

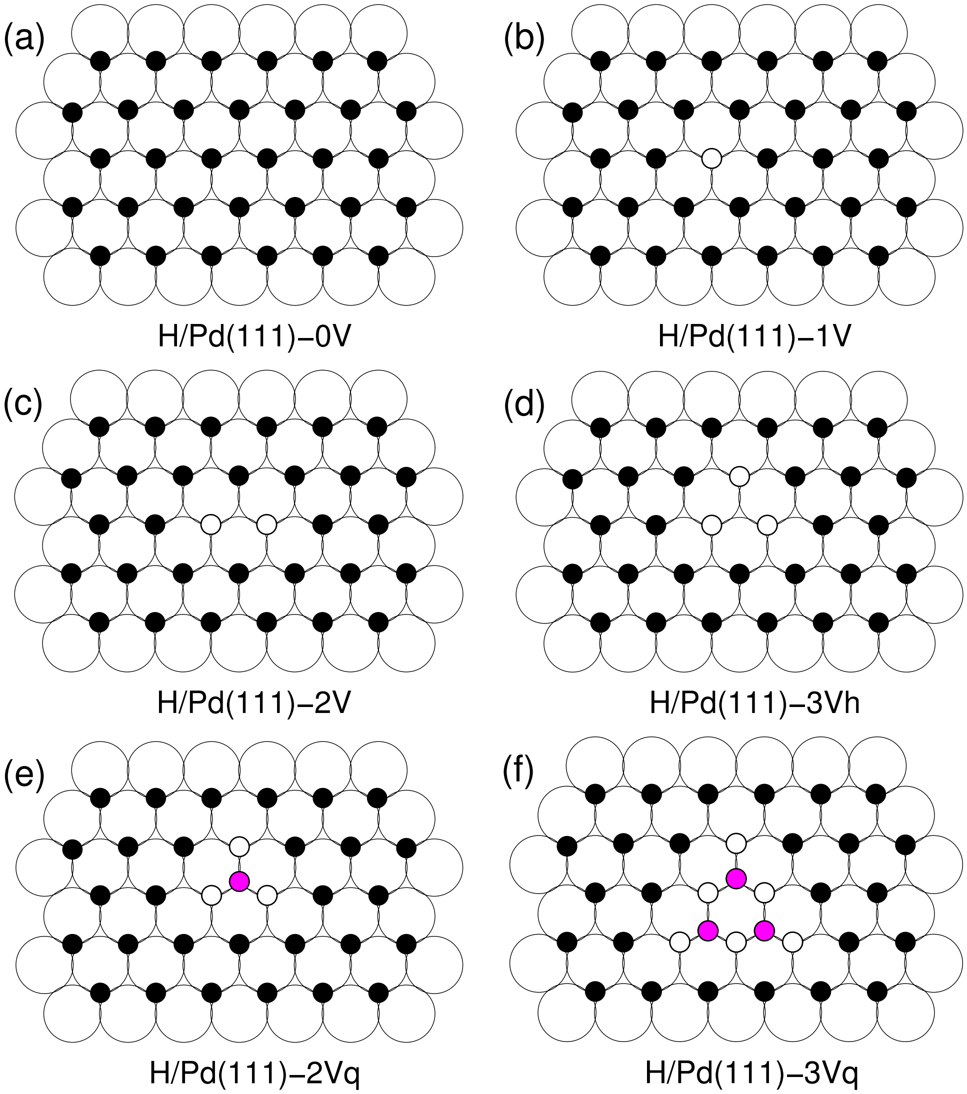

Figure 4.2 The hydrogen vacancy configurations considered in the present study. Pd atoms are represented by larger white circles and H atoms are represented by black circles. The smaller white circles represent empty fcc sites. The magenta (color) or gray (black and white) circles represent delocalized H atoms in the hcp sites. (a) No vacancy (0V), (b) single vacancy (1V), (c) two-vacancy (2V), (d) three-vacancy containing a single hcp site in the middle ($3V_H$). (e) two-vacancy defect ($2V_Q$) in the ground state. (f) Three-vacancy defect ($3V_Q$) in the ground state. $2V_Q$ contains three unoccupied fcc sites and one delocalized hydrogen atom occupies the central hcp site. $3V_Q$ contains six unoccupied fcc sites and three delocalized H atoms occupy three hcp sites.

fidently conclude that all hydrogen atoms in Fig. 4.2(e) other than the one in the middle of the vacancy defect are "locked" in their places and do not move other than making usual thermal oscillations about their equilibrium positions. Therefore, it is a very reasonable approximation that the problem of determining the minimum energy configuration of a two-vacancy defect is equivalent to solving Schrödinger equation for a single hydrogen atom moving in an external potential provided by H and Pd atoms in the configuration of $3V_H$ in Fig. 4.2(d).

The 3-dimensional potential energy surface (PES) is explored and mapped out by calculating the adsorption energy E_a of the H atom in question adsorbed at different positions over a $3V_H$ configuration. Since we need a potential representing an *isolated* $3V_H$ configuration, we constructed a $3V_H$ in a periodic 3×3 surface unit cell, which is bigger than any of the unit cell used in previous calculations that treated H atoms on metal surfaces quantum mechanically [31, 53]. The potential energy surface is explored according to the importance of each region: sample points are heavily populated near the "points of interest" such as the fcc sites, the hcp sites, and along the pathway between them while we sample less points away from these locations. Altogether over 3500 energy points populated in over 60 planes parallel to the Pd(111) surface are calculated. The planes are separated by 0.1 Å.

Fig. 4.3 and Fig. 4.4 show the PES for a single hydrogen formed by a $3V_H$ defect on Pd(111) surface. Fig. 4.3 is the contour plot of potential energy on a horizontal slice plane through the fcc adsorption site at which the global minimum is attained.

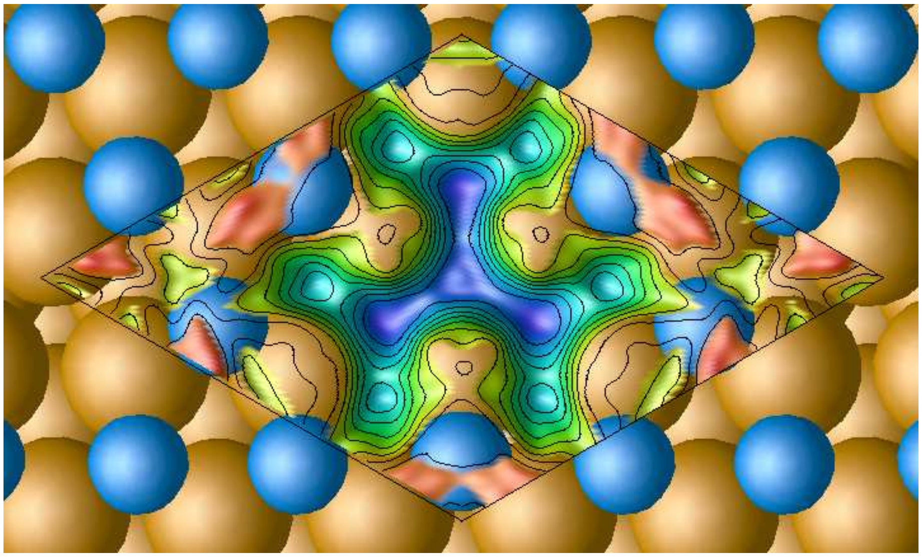

Figure 4.3 The potential energy on a horizontal slice plane through the fcc adsorption site at which the global minimum is attained. The potential is shown over 3×3 surface unit cell.

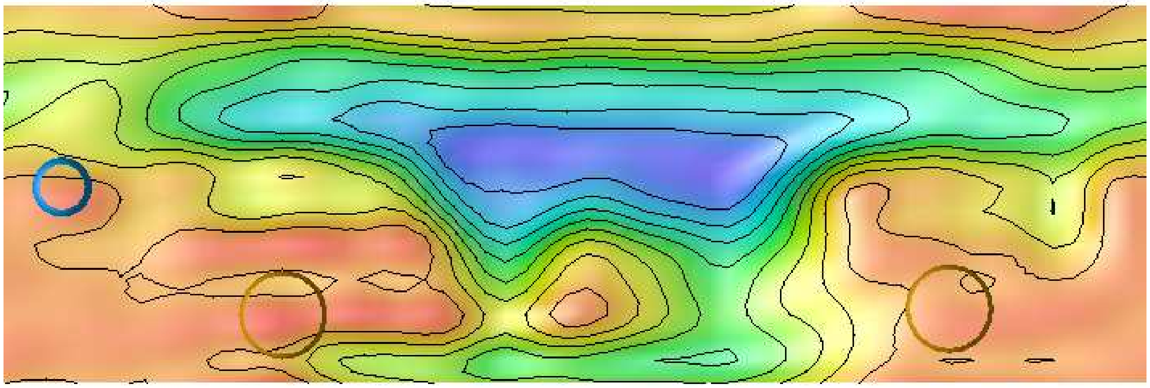

Figure 4.4 The potential energy on a vertical slice plane through the fcc adsorption site and hcp adsorption site. The minimum to the right is the fcc site and the minimum to the left is the hcp site. Local minimum energy sites in the sub-surface layer are also visible.

Fig. 4.4 shows the potential energy on a vertical slice plane through the fcc adsorption site and the hcp adsorption site. The PES is complex and highly anharmonic and possesses C_3 symmetry about the hcp site. There are four minima: at the hcp site in the middle and three fcc sites connected by narrow valleys. As given in Table 4.1, the minimum potential at the fcc site is lower than that of the hcp site by about 40 meV. Similar results are reported by previous calculations [59, 34] and our results are consistent with several experimental observations [9, 44, 47, 75].

4.2.6 Solving Schrödinger Equation

The Schrödinger equation for H atom is solved numerically in the momentum space. Although we are simulating a H atom moving in an isolated $3V_H$ defect, we still use periodic boundary conditions to take advantage of the Bloch theorem and the convenience of using plane waves as basis. To minimize the computational requirement in solving Schrödinger equation, we construct our unit cell to retain the full C_3 symmetry as well as the translational symmetry. As we report later, the wave functions for H atom in this unit cell is well confined inside of the potential well and has no tail across the barriers defining the potential well, thus indicating that the 3×3 surface unit cell we use is large enough to suppress the influence of neighboring cells to the H atom.

The wave function for the H atom is expanded in plane waves with kinetic energies up to 0.3 eV that includes 4529 plane waves. Due to large mass of H atom compared to electron mass, this cutoff energy is equivalent to more than 550 eV for electronic band structure calculations. Our tests show that the eigenvalues of H atom wave functions are well converged with this energy cutoff. As we simulate an isolated $3V_H$ defect with a large unit cell, the Brillouin zone is very small and k point sampling is not important. Indeed the eigenvalues for different k point shown in Fig. 4.5 exhibit very little dispersion.

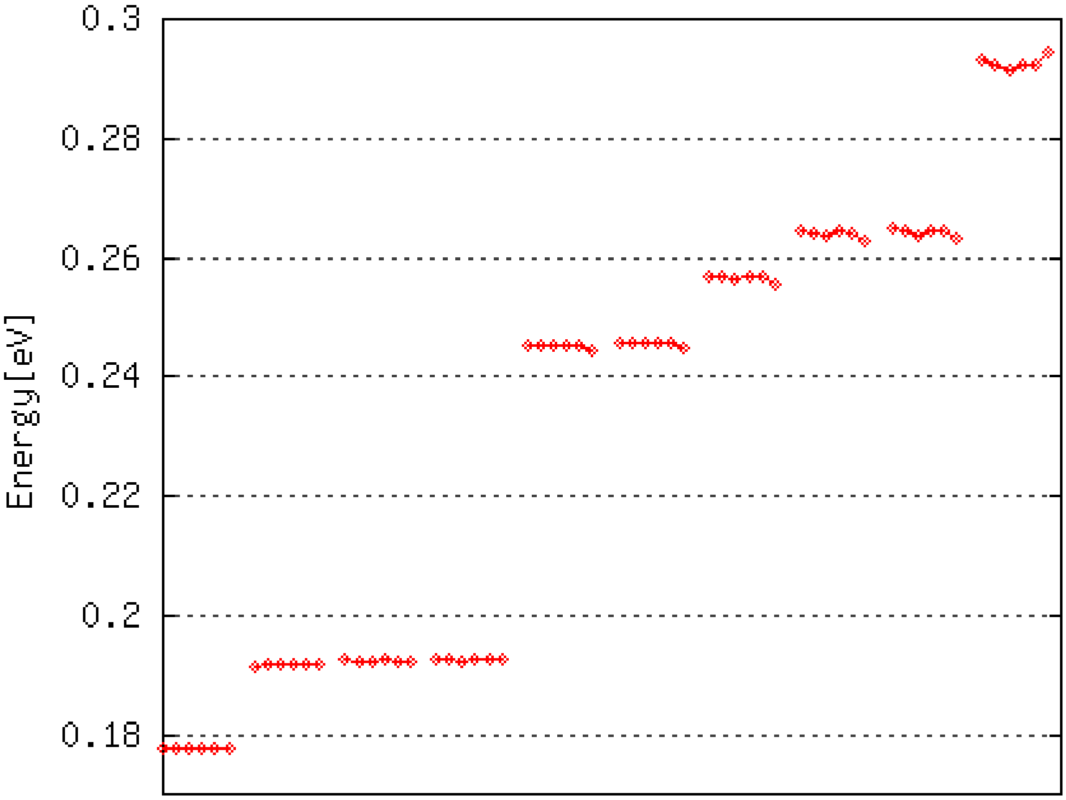

Figure 4.5 The eigenvalues on six different points in the Brillouin zone of an H atom chemisorbed inside of $3V_H$ vacancy defect. Eigenvalues are displaced horizontally to distinguish the degenerate eigenvalues.

4.3 Results and Discussions

4.3.1 Wave Functions for H Atom

Upon solving the Schrödinger equation for H atom moving in the potential well formed by $3V_H$ defect, we find wave functions showing substantial quantum effects as shown in Fig. 4.6 and Fig. 4.7. First few of the zero-point energy, measured from the bottom of the potential, for each state are 0.29 eV, 0.31 eV (triplet), and 0.37 eV (doublet). These values are comparable, but somewhat larger than the values previously reported under different configurations. For example, the ground state zero-point energy of 0.14 eV for nearly isolated H atoms on Pd(111) in 1/4 monolayer coverage has been reported by Källén and *et al*[31]. It is interesting, however, that the excitation energies for excited states computed from the zero-point energies are 20 meV and 80 meV. These values are smaller than 44 meV and 65 meV for H atoms in 1/4 monolayer coverage.

4.3.2 Ground State Structure for Vacancy Defects

However, the more interesting aspect of our result is the nature of the wave functions for the H atom. First, the ground state is broadly localized over the hcp site, not the fcc site where the potential is lower. Second, with small excitation energy of 20 meV, the H atom wave function can become a linear combination of the ground state and the excited states, which can be delocalized over the entire defect region.

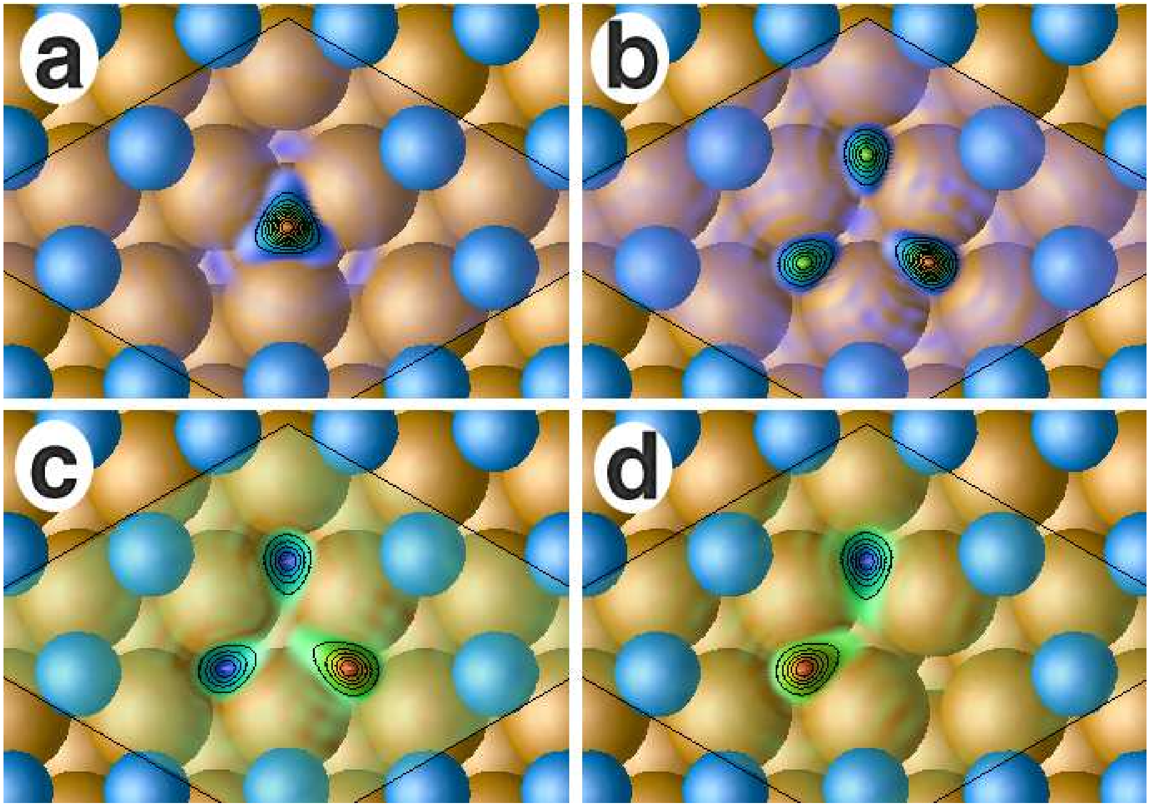

Figure 4.6 Real component of the wave functions for hydrogen atom on a horizontal slice plane through the fcc adsorption site: (a) ground state (ϕ_0) and (b-d) excited states (ϕ_1, ϕ_2, ϕ_3). All imaginary components are zero. The wave functions are evaluated at the center of the Brillouin zone. The eigenvalues for each state measured from the bottom of the potential are (a) 0.29 eV, (b-d) 0.31 eV with triple degeneracy. Pd atoms and H atoms are represented by gold and blue spheres, respectively.

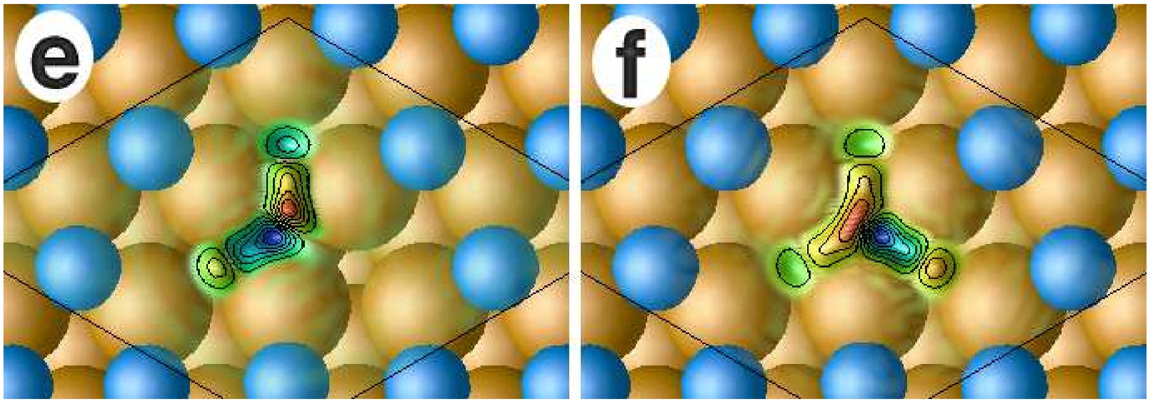

Figure 4.7 Real component of the wave functions for hydrogen atom on a horizontal slice plane through the fcc adsorption site: (a) fourth (ϕ_4) and (b) fifth (ϕ_5) excited state. All imaginary components are zero. The wave functions are evaluated at the center of the Brillouin zone. The eigenvalues for each state measured from the bottom of the potential are 0.37 eV with double degeneracy. Pd atoms and H atoms are represented by gold and blue spheres, respectively.

The fact that the ground state is localized in the hcp site rather than fcc site can be easily understood in terms of symmetry. Since the potential generated by $3V_H$ defect has C_3 symmetry about the hcp site, the ground state wave function must be an even and nodeless function with full C_3 symmetry about that point. With this symmetry, the ground-state wave function can minimize the kinetic energy by reducing the gradient of the wave function and overcome the deficit in potential energy. On the other hand, a wave function localized in one of the fcc sites, which can be constructed from the linear combination of the triplet excited states, has a nodal surface and therefore has higher kinetic energy.

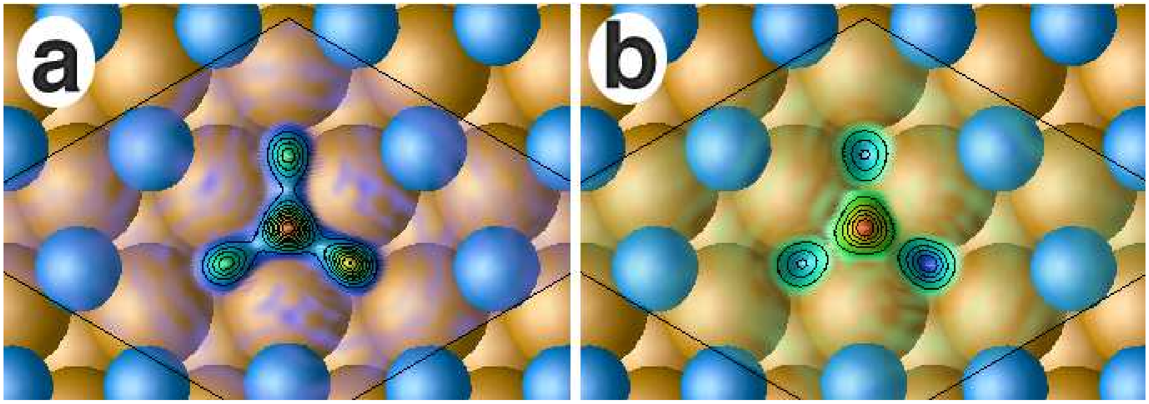

Figure 4.8 Examples of a linear combination of eigenstates. Real components of wave functions are shown. Imaginary componets are zero. (a) $\frac{1}{\sqrt{2}}(\phi_0+\phi_1)$, and (b) $\frac{1}{\sqrt{2}}(\phi_0-\phi_1)$. Pd atoms and H atoms are represented by gold and blue spheres, respectively.

The excitation energy of 20 meV is not much smaller than 37 meV, the differnece between the adsorption energy for fcc site and hcp site, which normally drives H atoms to occupy fcc sites instead of hcp sites. Therefore, we conclude that the ground-state structure for two-vacancy defect is the $2V_Q$ structure shown in Fig. 4.2(e). In other words, in a two-vacancy defect that has three unoccupied fcc sites and one hcp sites, the H atom occupies the hcp site and maximize its symmetry.

Given small excitation energy, the H atom wave function can acquire components of excited states. In Fig. 4.8 we show two examples of wave functions constructed from the linear combination of the ground state (ϕ_0) and one of the first triplet excited state (ϕ_1).

4.3.3 STM Image of Two-Vacancy Defects

Once the ground-state geometry is determined, it is very straightforward to interpret the STM image of two-vacancy defects. In fact, our model provides a very simple and direct explanation without resorting to the conventional thermal motion of H atoms between three fcc sites. We note that the H atom in Fig. 4.2(f) or Fig. 4.6(a) moves “out of the way” between STM tip and the fcc sites where, collectively, the tunneling current is strongest, partly due to the space left open by unoccupied fcc sites and partly due to the contribution from Pd atoms directly below the fcc sites. This enables STM tip to “see” all three fcc sites. Thus, the vacancy pair has the appearance of a bright triangle occupying three nearest neighbor fcc sites [76, 77].

4.3.4 Larger Vacancy Defects

The quantum effects that determined the ground-state goemetry of two-vacancy defect can now be generalized to determine the optimum structure of larger vacancy defects. Fig. 4.2(f) shows, for example, our model for the ground-state structure of a three-vacancy defect. There are six fcc sites and three hcp sites. Again, to maximize the symmetry and minimize the kinetic energy of the system the wave function of three H atoms will concentrate in the hcp sites. It is straight forward to show that for an n-vacancy defect, we will have $n_{\mathrm{fcc}} = n(n+1)/2$ fcc sites empty and $n_{\mathrm{hcp}} = n(n-1)/2$ hcp sites occupied by H atoms and their difference is $n_{\mathrm{fcc}} - n_{\mathrm{hcp}} = n$. Obviously, a rigorous way to verify our model for the gorund-state structure of a three-vacancy defect is to treat all three H atoms quantum mechanically in a potential formed by Pd atoms and neighboring H atoms in a $6\mathrm{V}_{\mathrm{H}}$ configuration. However, this potential energy surface is 9-dimensional (three for each H atom) and the surface unit cell needs to be at least four times bigger than the one used for the present study to adequately simulate an isolated triangular region created by six unoccupied fcc sites. Presently, this is impractically too large a calculation for today's computers. However, we have following two experimantal evidences that strongly support the validity of our proposed ground-state geometry of larger vacancy defects.

4.3.5 STM Image of Three-Vacancy Defects

First, our model again gives an excellent explanation for the observed STM images of three-vacancy defects. In a three-vacancy defect $3\mathrm{V}_{\mathrm{Q}}$ as shown in Fig. 4.2(f), all three

H atoms occupy the hcp sites leaving six fcc sites unoccupied. Again, the STM tip sees six “holes”, which correspond to six bright spots in STM images. The great advantage of this model compared to previously proposed rapid thermal motion of H atoms is that our model is based on the ground state structure of the defects themselves. STM images of defects are not the blurs caused by slow “shutter speed”, but they are what they actually look like.

Furthermore, the thermal motion model runs into a serious difficulty as the size of a defect increases. Let’s consider a three-vacancy defect according to this model as shown in Fig. 4.9. One possible starting configuration for 3V is shown in Fig. 4.9(a) where all H atoms are located at far corners away from each other. This is the only configuration that allows all three H atoms to have equal chance to make next move. In all other configurations, some atoms cannot move without going over large energy barrier. This energy barrier should be large enough to keep the H atoms on the edge of the triangular region from joining in and making the walls of the defect region to collapse. The fact that we can make well defined STM images of 3V defects ensures us that this is the case.

One of the next possible configuration is shown in Fig. 4.9(b) that is obtained when the lower left H atom (2) moves first into the left-middle position and then the right lower H atom (3) moves into the middle-bottom position as indicated by the arrows, *in the correct order*. At this configuration, only the H atom 3 can make the next move. All other atoms are locked in their places. So far, only H atom 2 and 3 have been moving. To argue that the random thermal motion of H atoms are the cause of six-ball triangular pattern for 3V, all

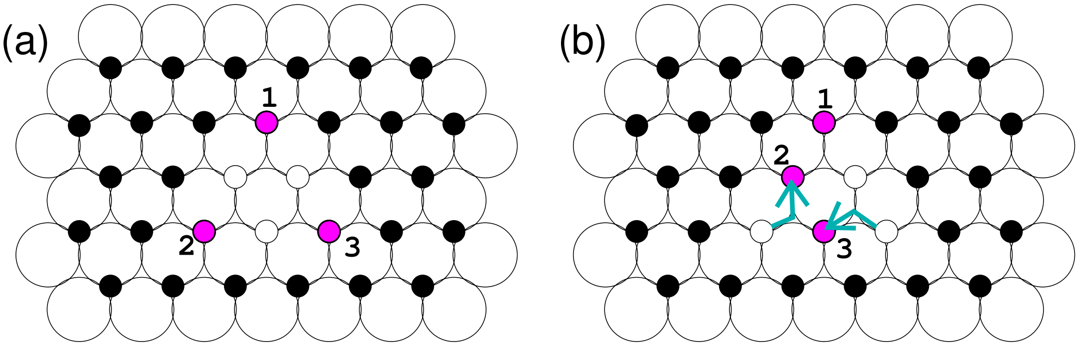

H/Pd(111)–3Vk

H/Pd(111)–3Vk–2

Figure 4.9 Difficulty in hydrogen vacancy defect model employing random thermal motion of H atoms. Pd atoms are represented by larger white circles and H atoms are represented by black circles. The smaller white circles represent empty fcc sites. The magenta (color) or gray circles represent hot H atoms moving around in the defect. (a) A possible starting configuration for 3V defect. All H atoms are located at far corners away from each other where they don't interfere with the movement of other H atoms. (b) Next possible configuration when the lower left H atom (2) moves first into the left-middle position and then the right lower H atom (3) moves into the middle-bottom position as indicated by the arrows, *in the correct order*. At this configuration, only the H atom 3 can make the next move. All other atoms are locked in their places.

three atoms must move around equally. Before H atom 1 can have any opportunity to make a move, *both* H atom 2 and 3 must move back to the bottom positions. In order for that to happen, in the fewest moves, H atom 3 must undo his move and go back to his original place first and them H atom 2 can choose the middle or left bottom position. This requires extraordinary coordination among H atoms and severly limit the frequency that all six fcc sites are visited uniformly. According to this model, it should be possible that some H atoms do not get to move much and we should occasionally observe a 3V defect assumes an elongated shape rather than a perfect equilateral triangular shape. However, none of the previously reported STM images show any other shape than a perfect equilateral triangular shape[76, 77].

4.3.6 Inactivity of Two-Vacancy Defects

The second experimental evidence that supports our model is related to the dissociative adsorption of H_2 molecules via vacancy defects on a Pd(111) surface.

In fact, the most unexpected result of the experiment by Mitsui and *et al* was that aggregates of three or more hydrogen vacancies are far more efficient in H_2 dissociation while two-vacancy sites are virtually inactive[76, 77]. This is totally contrary to conventional Langumir principle that two active sites in close proximity should be sufficient to facilitate the dissociation of a H_2 molecule containing two H atoms. This has been baffling many scientists and yet no clear answer has been put forward to date. Our quantum mechanical model for the ground-state structure for vacancy defects provides a clear answer to this puzzle.

Fig. 4.10 demonstrates the difference between two-vacancy defects and larger vacancy defects. According to our quantum calculations, the H atoms in the defect occupy the hcp sites and its ground state wave function is localized in the hcp sites. However, the wave function is rather broad and delocalized over substantial area reaching to the fcc sites as shown in Fig. 4.6(a). Furthremore, with small excitation energy, the first triplet excited states can be mixed in the H atom wave function. One such example is shown in Fig. 4.8. Although the main portion of this wave function is concentrated in the hcp site, it covers the most of the entire triangular region. Therefore, we can say that the delocalized H atom in the hcp site "occupies" the entire triangular area defined by three fcc sites around the hcp site.

In Fig. 4.10, we indicated the region occupied by each of the delocalized H atom in the hcp sites. Immediately a clear picture emerges. In $2V_Q$ defect, the entire defect area is occupied by the H atom in the hcp site. In $3V_Q$ defect, three H atoms occupy three triangular regions, but leave a big hole in the middle. The area left "unoccupied" is one fourth of the total defect area. Furthermore, the center of this unoccupied area is the top site that has the highest symmetry providing an ideal location for a H_2 molecule to be physisorbed and form a precursor state. Once a precursor state is formed, H_2 molecule has very high probability to be adsorbed into the defect. The fact that the exposed area contains the top site is also very significant. Dong and *et al* used the first-principles method

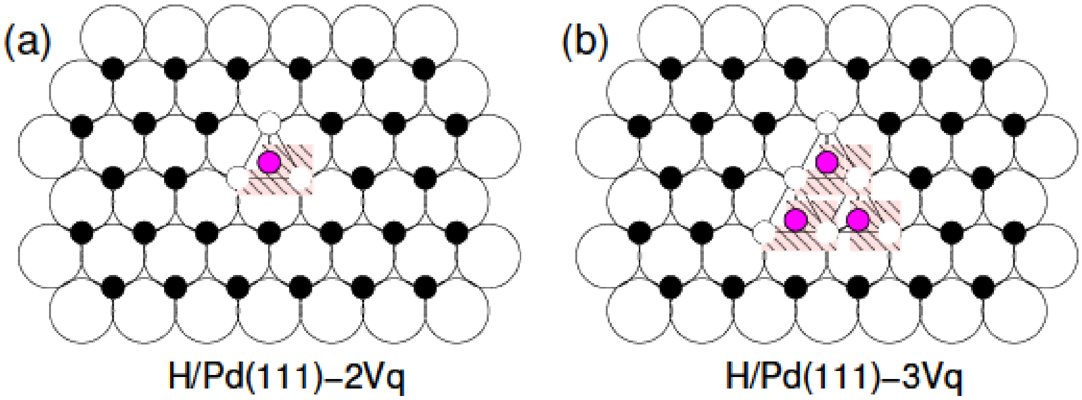

Figure 4.10 Adsorption of H_2 molecules on 2V and 3V defects. Pd atoms are represented by larger white circles and H atoms are represented by black circles. The smaller white circles represent empty fcc sites. The magenta (color) or gray (black and white) circles represent delocalized H atoms in the hcp sites. The triangles represent the area occupied by the delocalized H atoms. (a) Two-vacancy defect. (b) Three-vacancy defect.

to study the dissociative adsorption of a single H_2 molecule on a clean Pd(111) surface and reported that they found the existence of a precursor state over the top site[81]. Olsen and *et al* reported that the adsorption path of H_2 molecule on Pt(111) surface over the top site has no barrier to hydrogen dissociation[66, 3].

On the contrary, for a $2V_Q$ defect, the point of highest symmetry is already taken and there is no particular point that stands out as a candidate for H_2 molecule attachment. In this regard, $2V_Q$ defect is so symmetric and widely covered by H atom, it can be considered even *less active* than a single-vacancy defect, which is practically inactive for H_2 dissociation and adsorption.

4.4 Summary

We determined the ground state structure of two-vacancy defect of H atom on a Pd(111) surface by treating the motion of a H atom quantum mechanically in the vicinity of the defect. We solved Schrödinger equation for a single H atom moving in static potential energy surface that has been mapped out by first-principles density-functional theory calculations. We find that a H atom in the vicinity of a two-vacancy defect experiences substantial quantum effects and its wave functions are delocalized over large portion of the defect. Our results indicate that the ground-state wave function is concentrated in the hcp site rather than the fcc site where H atoms normally settle. We show that symmetry plays a major role in the reversal of the order of the most enegetically favorable site. Our results explain the STM images of two- and multi-vacancy defects with ground-state properties of the defects. More importantly, our model also provides a simple and clear argument in elucidating the high activity of three- or larger defects in hydrogen molecule dissociation and the inactivity of two-vacancy defects.

CHAPTER V

FIRST PRINCIPLE STUDY OF SEMICONDUCTOR SURFACES

5.1 Introduction

The surface reconstruction and adsorption of atoms on reconstructed surfaces play pivotal roles in understanding the epitaxial growth of semiconducting materials [80, 56, 82]. The III-V semiconductors have a zinc-blend crystal structure made of group-III atoms and group-V atoms. One particular family of III-V semiconductors—namely, InAs, GaSb, AlSb, and their related alloys—is called “6.1 Å” semiconductors because they all have lattice parameters very close to this value. When thin layers of different III-V semiconductors are grown in an alternating fashion using techniques such as molecular beam epitaxy (MBE), the materials scientists classify them as III-V semiconductor heterostructures. Because of their near-match lattice parameters and the same crystal structure, materials scientists can combine different sets of III-V semiconductors to produce materials with a variety of band alignments. The “6.1 Å” family of semiconductors are combined to heterostructures to fabricate a variety of technologically important devices such as field effect transistors [39], resonant tunneling structures [20, 41], infrared lasers [55], and infrared detectors [21].

Cross-sectional scanning tunneling microscopy (XSTM) has emerged as a powerful technique to characterize III-V semiconductor heterostructures [58, 70, 67, 1, 33, 22, 37, 56, 14, 71, 6]. Precise characterization of these materials is made possible by the fact that a zinc-blend III-V crystal readily cleaves along the $\{110\}$ faces, producing a nearly defect-free surface that presents a cross-sectional view through a single lattice plane of structures grown on (001) substrates.[58] Tunneling microscopy is particularly useful for III-V (110) surfaces because of the simple surface structure, illustrated in Fig. 5.1(a).

The III atoms relax towards the surface and V atoms away, shifting charge between the atoms and leaving the III dangling bond essentially empty and the V surface orbital filled. Because the STM surface topography in constant-current images approximately corresponds to contours of constant integrated charge density, only the III dangling bonds are seen in empty-state images of III-V $\{110\}$ surfaces, while V orbitals are seen in filled-state images.[22, 19] Therefore, XSTM images provide an apparently straightforward chemical identification of the atoms observed.

Since the first report of atom-selective STM images of GaAs(110),[22] and the observation of a heterostructure using XSTM,[58] a major issue has been delineating between electronic and geometric sources of height contrast. For nominally homogeneous materials where isolated impurity atoms are observed, such as dopants or substitutional defects, electronic origins of contrast have dominated the discussions.[18] For heterostructures, there are three contrast issues to be considered. First, the different III-V materials in a heterostructure usually have a different topographic height in filled-state im-

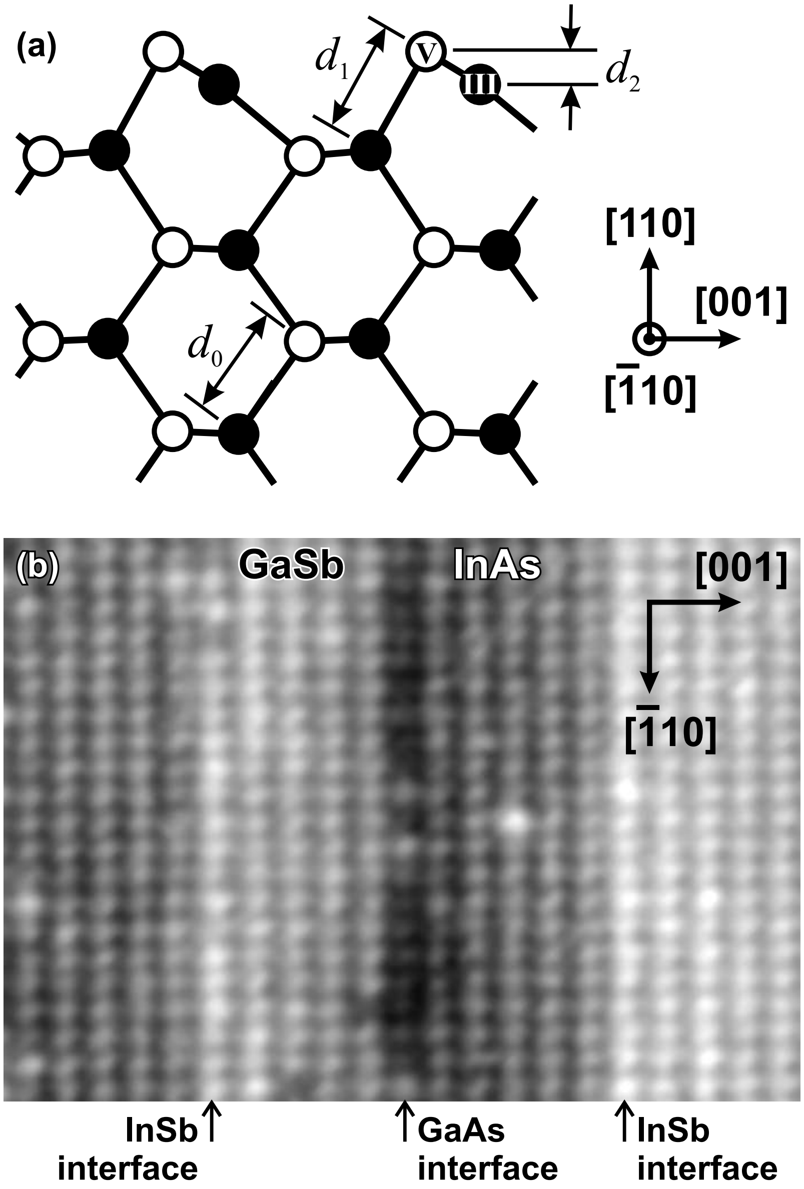

Figure 5.1 (a) Relaxed geometry of a III-V (110) surface. d_0 denotes the bond length in the bulk, d_1 the out-of-plane III-V bond length indicated, and d_2 the height difference between III and V surface atoms. (b) Constant-current, filled-state XSTM image of an InAs/GaAs superlattice.

ages. Until the past few years,[22, 37, 56, 14, 71] discussion of this difference focused on electronic effects, specifically on the band gaps and band alignments (for filled states, the valence band maximum), and the associated number of bands contributing to the tunneling.[58, 70, 67, 1, 33] The second contrast issue is related to the relative appearance of point defects associated with inter-diffusion between the materials. For example, Harper *et al.* originally described As defects in GaSb as appearing lower in height because of the position of the As HOMO.[33] Finally, there is the local height of interfacial bonds to consider. For systems without a common anion, such as InAs/GaSb, two different types of interfacial bonds are possible (InSb and GaAs bonds in this case), and it has recently been proposed, based on crystallographic arguments, that the local XSTM height is primarily determined by local bond lengths.[37, 56]

It is a well documented fact that the compositional and structural variations at the interfaces can dramatically affect the transport and optical properties of semiconducting heterostructures [28, 5, 10]. The atomic-scale understanding of the formation of interfaces in III-V heterostructures, such as GaSb/InAs, is critically important for the advancement of the micro-electronic device technology. This knowledge will allow us to control the composition of interfacial bond types and reduce defects at interface. The adsorption of As and In atoms on the surfaces of GaSb semiconductor is very much relevant to the initial stage of molecular beam epitaxy (MBE) growth of an InAs film on a GaSb substrate. The full understanding of adsorption process, in turn, cannot be obtained without extensive knowledge of the structure of the surfaces where these adsorption processes take place.

In this work we use first-principles methods to describe the electronic and geometric structure of the (110) surfaces of InAs/GaSb superlattices. We find that the apparent surface height difference between the two materials is primarily an electronic structure effect, but the local height differences observed for InSb and GaAs interfacial bonds are mostly geometric in nature. In addition, the calculations reveal that atomic intermixing lowers the energy of GaAs interfaces, favoring disorder. We also study the atomic-scale structures that determine the reconstruction of the (001) surfaces of GaSb semiconductors and the adsorption of In and As atoms on these surfaces. Surface reconstruction on two different types of (001) surfaces, namely Ga- and Sb-terminating surfaces, are considered. We observed that both surfaces showed strong dimerization of surface atoms. Ga-terminating surfaces exhibited substantial buckling of surface atoms, while Sb-terminating surfaces did not show any appreciable buckling. Our calculations showed that arsenic atoms would be preferably adsorbed at the bridge site between the dimerized Sb atoms on Sb-terminating surfaces. On Ga-terminating surfaces, on the other hand, In atoms were observed to have more or less equal probabilities to be adsorbed at several different sites. Our calculated energies for atomic inter-diffusion indicate that anion exchanges are exothermic for As atoms on Ga-terminating (001) interfaces but endothermic for In atoms on Sb-terminating (001) interfaces. This difference is consistent with the experimental observation that GaAs interfaces are typically more disordered than InSb interfaces in III-V heterostructures.

5.2 Experimental Method

The XSTM measurements were performed in ultra-high vacuum using InAs/GaSb superlattice samples grown by solid-source molecular beam epitaxy, as described in detail previously.[56] All images presented here are of (110) surfaces recorded with filled states at constant current (2.2–2.5 V, 150–200 pA).

Fig. 5.1(b) shows a typical filled-state XSTM image for a (110) surface. In our theoretical work, we focus on three aspects of this representative image. First, the large-scale topography shows an alternating pattern of brighter and darker bands (higher and lower apparent heights) corresponding to GaSb and InAs layers, respectively. Second, a higher Sb row is evident at InSb interfaces in this figure, whereas a lower As row is evident at the GaAs interface. Third, the degree of atomic disorder at the two interfaces is qualitatively different: InSb interfaces typically appear atomically abrupt, in contrast to GaAs interfaces which often exhibit significant disorder.

5.3 Computational Method and Details

Our calculations are based on the first principles density-functional theory (DFT) [62, 48], using ultrasoft pseudopotentials as implemented in the VASP code.[16, 25, 24] Exchange-correlation effects were treated within the local-density approximation (LDA) as parametrized by Ceperly and Alder [15]. The wave function of electrons are expanded in terms of plane-wave basis set [52], and all plane waves that have kinetic energy less than 150 eV are included in expanding the wave functions. The structure optimizations were performed until the energy difference between successive steps becomes less than 10^{-4} eV.

5.4 Cross-Sectional STM Calculations

Our sampling of the Brillouin zone for cross-sectional STM calculations was equivalent to using 64 *k*-points in the full zone of the primitive fcc cell. We used supercell geometries to represent the InAs/GaSb heterostructures. Because of the importance of interfacial strain in this material system, we constructed supercells with starting geometries that minimized, as much as possible, any artificial strain at the interfaces. Our procedure consisted of the following three steps. (1) Bulk calculations were performed to obtain the optimized lattice parameters for four different types of zinc-blend III-V semiconductor crystals: InAs, GaSb, InSb, and GaAs. (2) For each of these four different homogeneous materials, we constructed slab supercells representing the unreconstructed (110) surfaces. This was done by periodically replicating the unit cells obtained in the previous step four times along the (110) direction, resulting in slabs containing eight atomic layers. We separated adjacent slabs by a vacuum region corresponding to five atomic layers, which we confirmed was sufficient to make the interaction between slabs negligible. All of the atoms within each slab were then relaxed within the constraint of the fixed in-plane lattice constant determined from the previous step. (3) Next we periodically replicated the relaxed slabs six times along the (001) direction, and joined two such extended slabs together to form various III-V heterostructures with (001) interfaces and exposed (110) surfaces. For each interfacial bond case (InSb and GaAs), the two slabs were joined at a distance chosen as to allow every interfacial bond to have a bond length corresponding to the bulk lattice constant computed in step (1). The resulting supercells each contained a total of 96 atoms, with four different atomic species, corresponding to a (001) superlattice period of 24 atomic layers. Finally, the positions of all atoms were completely relaxed within the constraints of fixed superlattice period and fixed lattice constant along $[1\bar{1}0]$.

Table 5.1 Lattice constants, a_0, and bond lengths, d_i, of the relevant III-V materials, in Å. See Fig. 5.1(a) for definitions of the different bond lengths. a_0^1 indicates lattice constant from this work, a_0^2 indicates experimental lattice constant.

	a_0^1	a_0^2	d_0	d_1	d_2
InAs	6.01	6.06	2.60	2.62	0.77
GaSb	6.04	6.10	2.62	2.65	0.76
InSb	6.43	6.47	2.78	2.80	0.86
GaAs	5.60	5.65	2.42	2.44	0.70

The equilibrium lattice constants calculated in step (1) are listed, along with their experimental values, in the first two columns of Table 5.1. The agreement is very good, with all errors less than 1%. The relaxed (110) surfaces of the four homogeneous materials, as obtained from step (2), show the surface buckling obtained in many previous studies[19]. The calculated buckling, illustrated in Fig. 5.1(a) and tabulated in the last three columns of the table, is in good quantitative agreement with experiment; in particular, the height difference between III and V atoms for InAs is 0.77 Å, in excellent agreement with the value of 0.78 Å determined by low-energy electron diffraction [54].

After relaxing the various III-V heterostructures described in step (3), we simulated XSTM images using the method of Tersoff and Hamann. [78] To simulate filled-state images, we integrated the local density of states (LDOS) from 1 eV below the Fermi level up to the Fermi level; the surface of constant integrated LDOS then corresponds to the ideal STM topography.

Our results for InAs/GaSb heterostructures with InSb interfacial bonds are shown in Fig. 5.2. The geometry of the fully relaxed (110) surface is displayed in Fig. 5.2(b). As in the case of homogeneous structures, the surface atoms buckle, causing the Group-V atoms (As and Sb) to move outward and the Group-III atoms (In and Ga) to move inward. At the interface, Sb atoms relax still further outward so as to partially relieve compressive strain in the InSb bonds. The resulting simulated XSTM image closely resembles the measured image, as indicated by the inset of Fig. 5.2(a) and the calculated XSTM profile across the row maxima shown in Fig. 5.2(c). Away from the interface, the topographic maxima (from the integrated LDOS) are 0.15 Å higher on the GaSb than on the InAs, in good agreement with the height difference of about 0.2 Å typically observed in XSTM images.

Interestingly, the difference in height between the actual Sb and As atoms associated with the topography is much smaller, 0.06 Å, demonstrating that the XSTM height difference is primarily caused by the surface electronic structure. Based on the calculated structure, the opposite appears true for the local topographic height difference observed at

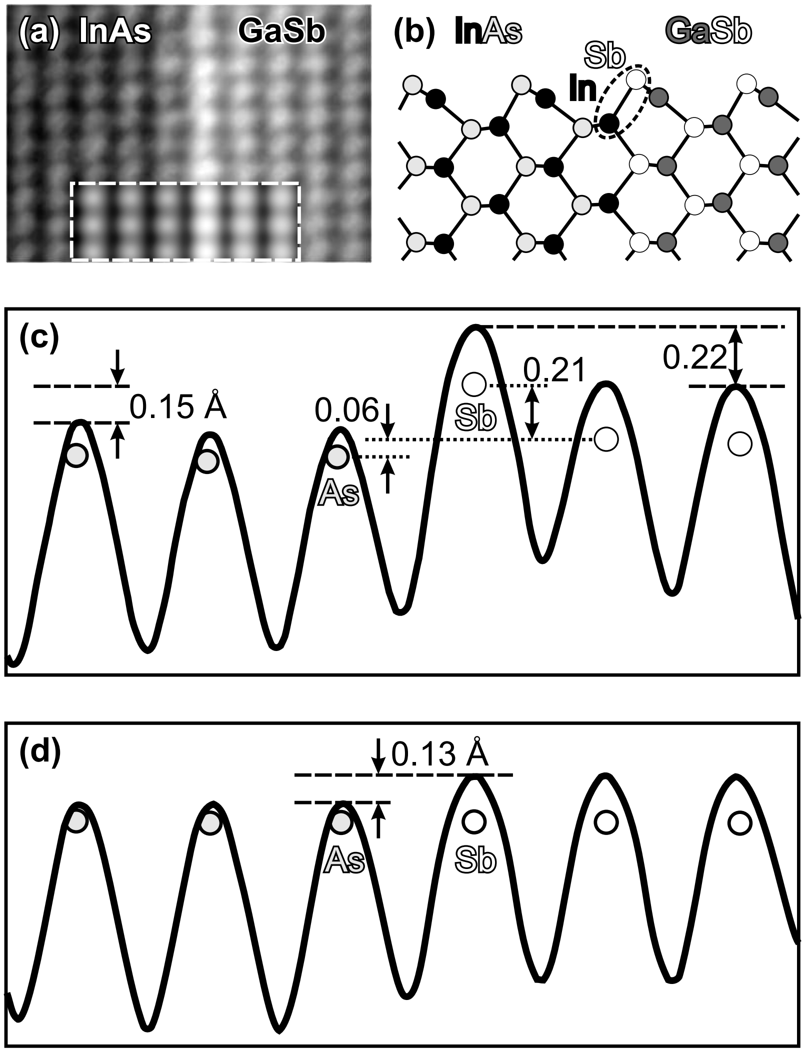

Figure 5.2 (a) XSTM image of an InAs-GaSb interface with InSb interfacial bonds. INSET: Simulated XSTM image of this structure. Both gray scales span about 1 Å. (b) Side view of the fully relaxed surface geometry for this interface. (c) Line profile for the simulated image along the [001] direction (across the row maxima). Circles denote the relaxed positions of the surface As and Sb atoms. (d) Line profile for a simulated image of two homogeneous structures joined together at their ideal lattice positions and allowed to relax the electronic but not the geometric structure.

the InSb interface. The Sb row forming InSb bonds is geometrically higher by about 0.2 Å than the Sb atoms on the GaSb surface, essentially the same height difference that occurs in the integrated LDOS, demonstrating that the observed height difference in this case is associated with the geometric structure.

In order to more explicitly delineate the relative contributions of geometric and electronic structure relaxation on the apparent STM topography, we calculated the electronically-relaxed structure of an "ideal" InAs/GaSb heterostructure, with all interfacial atoms frozen at ideal positions. In this ideal geometry all atoms in the top layer have exactly the same height, and thus differences in heights across the computed topography originate from purely electronic effects. As shown in Fig. 5.2(d), the electronic structure alone creates a difference in height of 0.13 Å between the InAs and GaSb surfaces, close to the 0.15 Å difference calculated with full relaxation, further supporting our conclusion that electronic structure underlies the measured height difference between the two materials.

Our analogous results for InAs/GaSb heterostructures with GaAs interfacial bonds are summarized in Fig. 5.3, with the calculated topography again in qualitatively good agreement with that observed experimentally. At this interface the structural relaxation is quite different from the InSb case. As shown in Table 5.1, GaAs bonds have the shortest surface bond length, d_1, and thus As atoms near the interface relax even further inward than Sb relaxes outward at InSb interfaces. The resulting geometric height of the As row at the GaAs interface is 0.24 Å lower than the As atoms far from the interface. However, as we saw at the InSb interface, the computed topographic height difference is almost identical,

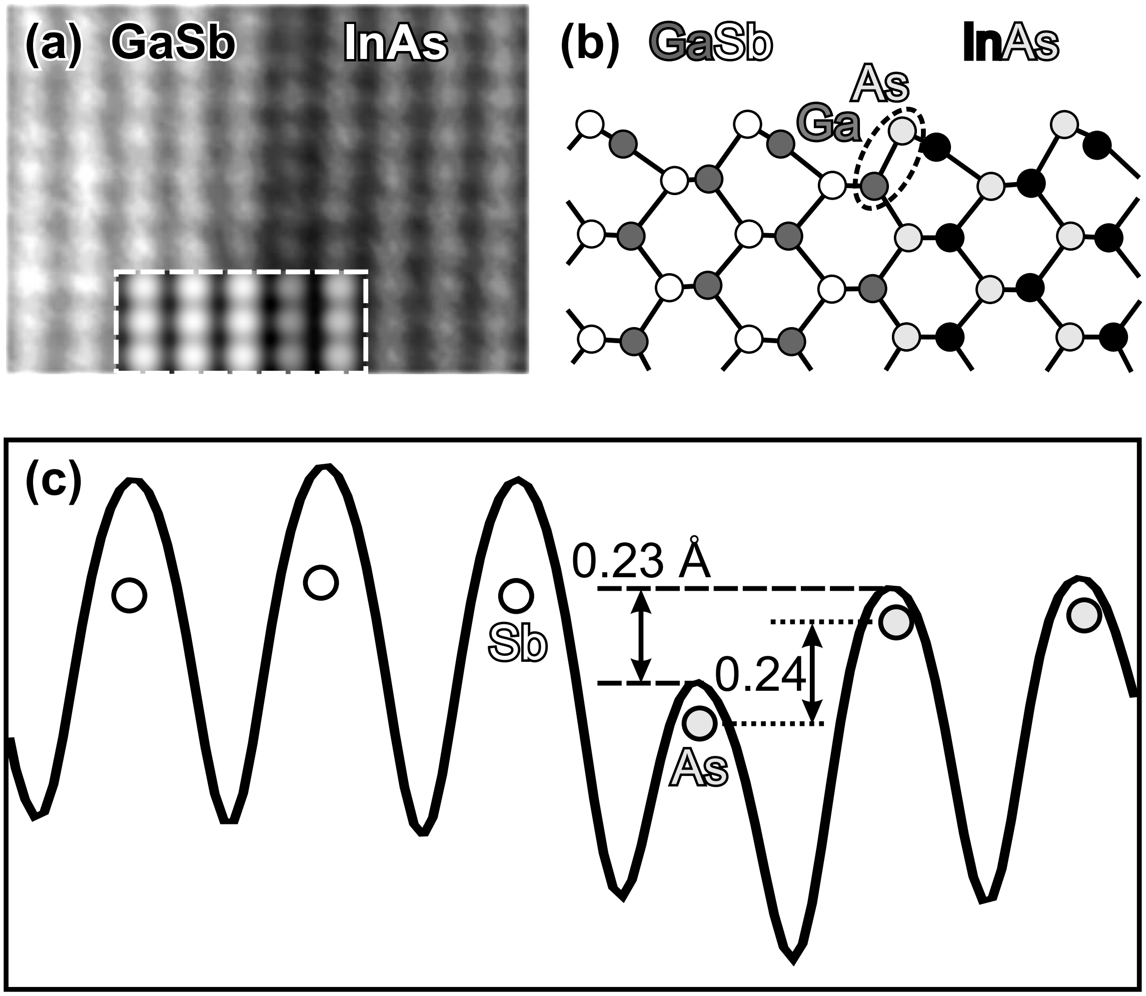

Figure 5.3 (a) XSTM image of an InAs/GaSb interface with GaAs interfacial bonds. INSET: Simulated image of this structure. (b) Side view of the fully relaxed surface geometry for this interface. (c) Line profile for the simulated image along the [001] direction.

0.23 Å, indicating that the local depression of the GaAs interface is almost completely geometric in origin.

Finally, we address why interfacial roughness appears to depend on the interfacial bond type, with GaAs interfaces generally observed to be more disordered. Experimentally, most defects occur close to the interfaces, suggesting that they arise from simple Ga-In or As-Sb exchanges across the interface, rather than from bulk defects such as vacancies or cation-anion antisites. An example of an apparent Sb atom observed in an As site at a GaAs interface is highlighted in Fig. 5.4(a). To confirm the structural assignment of such features, we theoretically modeled such a defect by replacing one of the surface As atoms at a GaAs interface with an Sb atom, as illustrated in Fig. 5.4(b). The simulated XSTM image for this structure, shown in the inset of Fig. 5.4(a), closely resembles the experimental result.

To investigate the energetics of anion interfacial defects, we consider the simplest defects that both preserve the global stoichiometry and satisfy local chemical bonding requirements, As-for-Sb exchanges. Such exchanges represent a simple mechanism for interfacial disorder at a nominally abrupt interface. We studied the energetics of exchanging adjacent As and Sb atoms both at an InSb interface and at a GaAs interface, as shown in Figs. 5.4(c) and 5.4(d), respectively. The structures were fully relaxed before and after the exchange and the change in the total energy then computed. At the InSb interface, the exchange raised the total energy by 7 meV. Surprisingly, at the GaAs interface, the same process actually *lowered* the total energy by 22 meV; i.e., the formation of such defect

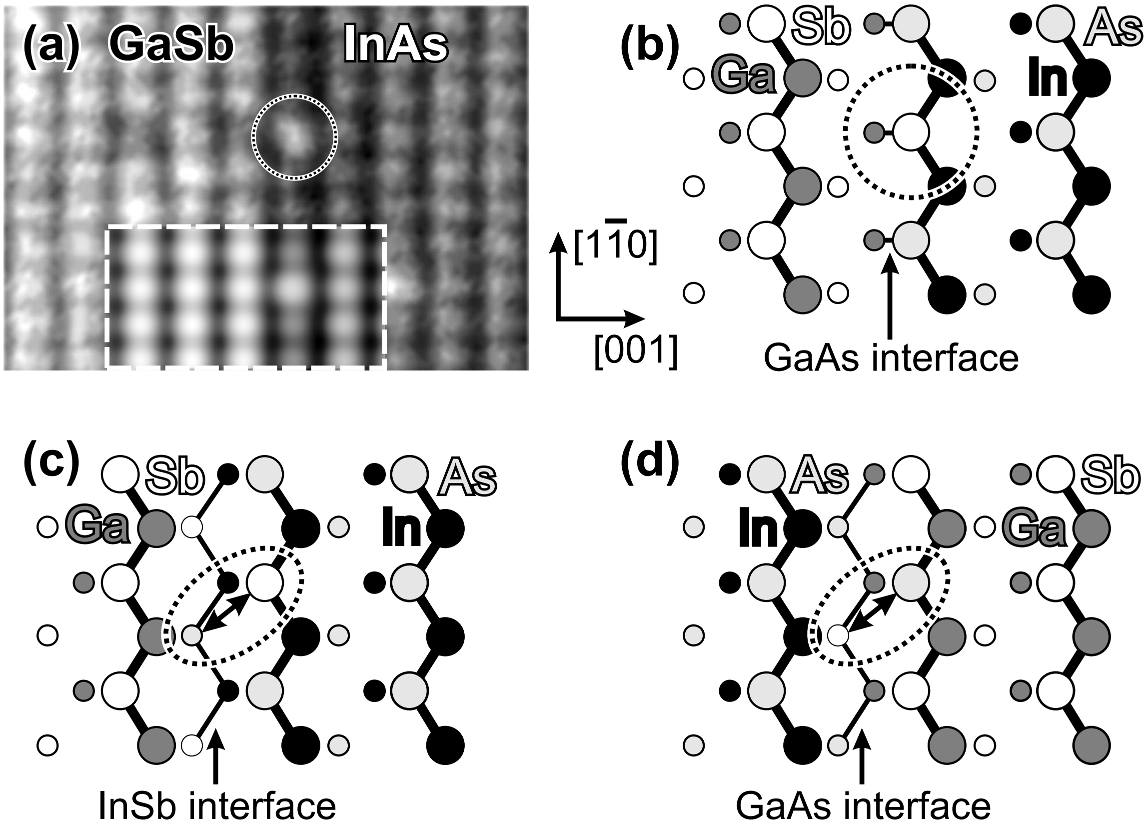

Figure 5.4 (a) XSTM image of InAs/GaSb with a GaAs interface. An apparent Sb atom in an As site at the interface is circled. INSET: Simulated XSTM image for such a defect. (b) Top view of the Sb-in-As-site defect model structure, with the top-layer atoms shown larger. (c) Model used to calculate the energetics of an As-Sb exchange across an InSb interface. (d) Model for an As-Sb exchange across a GaAs interface.

pairs is *exothermic*. This result implies that abrupt GaAs interfaces are thermodynamically unstable. Therefore, although kinetic barriers may suppress anion exchanges, one should generally expect GaAs interfaces to be more disordered than InSb interfaces (as widely observed). This point will be further elaborated in Sec. 5.5.3 when we investigate the inter-atomic exchange diffusion during thin film growth process.

5.5 Adsorption on Interface Surfaces

Our sampling of the Brillouin zone for these calculations was equivalent to using 231 k-points in the full zone of the primitive fcc cell. We used supercell geometries to represent a GaSb semiconductor slab containing two different surfaces as illustrated in Fig. 5.5.

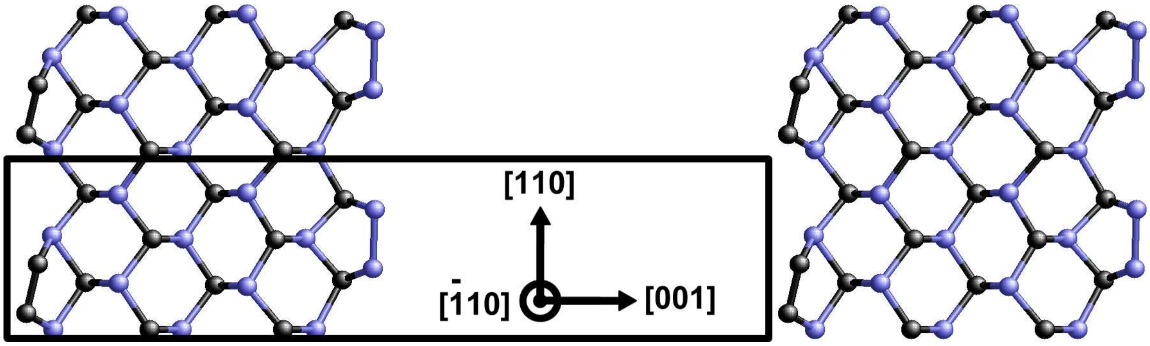

Figure 5.5 Supercell geometry containing GaSb semiconductor slab. A fully optimized structure is shown. The solid line rectangular box indicates the unit cell used for present calculations. Blue (lighter gray in gray scale figures) spheres represent Sb atoms while black spheres represent Ga atoms.

Again, the supercell was carefully prepared to have a starting geometry with minimum artificial strain. Using the optimum bulk structure obtained in the previous calculations, we first constructed slab supercells representing the unreconstructed (001) surfaces. This was done by periodically replicating the unit cell used in the GaSb bulk structure calculation along the [001] direction, resulting in slabs containing twelve atomic layers.

We separated adjacent slabs by a vacuum region corresponding to twelve additional atomic layers, which we confirmed was more than sufficient to make the interaction between neighboring slabs negligible. To ensure we had enough layers of atoms across each slab, we inserted an additional pair of atomic layers of GaSb and repeated the same calculation for surface reconstruction. The added layers made no appreciable changes to all relevant physical quantities we monitored, confirming that the thickness of the slab was sufficient to reduce the interaction between the atoms on opposite sides of the same slab to a negligible level.

Fig. 5.6 shows the size of the unit cells in (001) planes. The unit cell contains enough atomic layers in lateral directions, [110] and [$\bar{1}$10], to allow up to (2×2) surface reconstruction. This was achieved by periodically replicating the unit cells along both [110] and [$\bar{1}$10] directions twice.

5.5.1 Surface Reconstruction

By having an even number of atomic layers in the slab, as shown in Fig. 5.5, we were able to simulate the reconstruction of two different types of surfaces of GaSb semiconduc-

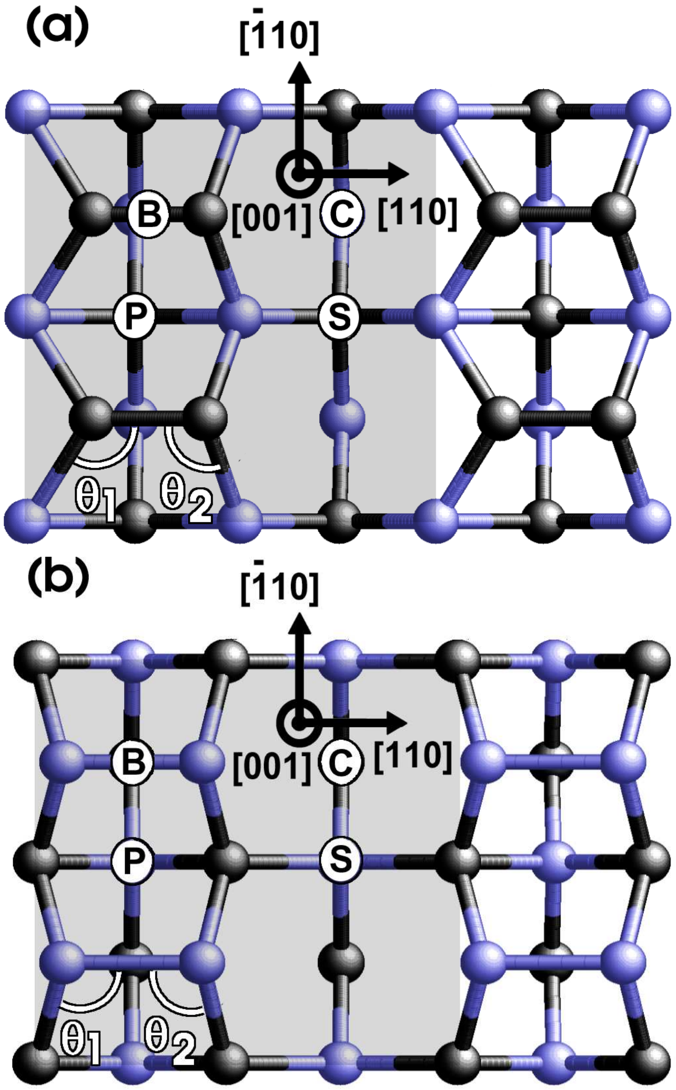

Figure 5.6 Reconstructed surfaces viewed from the top([001] direction). (a) The Ga-terminating surface and (b) Sb-terminating surface. The shaded areas indicate the (2×2) unit cells used for present work. Marked positions are four of the typical adsorption sites: (B) “bridge” site, (P) “pedestal” site, (C) “cave” site, and (S) “saddle” site. See text for detailed definition of each site. There are second sets of these four adsorption sites (not marked) in the other halves of the unit cells making the total of eight available adsorption sites. Refer the caption of Fig. 5.5 for coloring scheme.

tors at the same time. We found that Ga-terminating surfaces, the left side surfaces of the slabs in Fig. 5.5, exhibit dimerization. Fig. 5.6(a) also shows the top view of the reconstructed but bare Ga-terminating surface. Pairs of surface Ga atoms form dimers doubling the periodicity along [110] direction. These dimers also tend to tilt from (001) planes by about 15° causing the surface to buckle. As a result, one of the Ga atoms was pulled in toward the plane of the underlying Sb atomic layer and formed a planar structure with two Sb atoms and the other Ga atom.

Sb-terminating surfaces, the right side surfaces of the slabs in Fig. 5.5, also show dimerization. The top view of the Sb-terminating surface is shown in Fig. 5.6(b). Sb dimers on Sb-terminating surfaces, however, behave quite differently in terms of buckling. The Sb dimers do not tilt from (001) planes and stay parallel to the surface. These behaviors can be explained by considering the average number of valence electrons associated with surface atoms and the formation of hybrid orbitals. Ga atoms are group III atoms with three valence electrons, while Sb atoms are group V atoms with five valence electrons. In bulk GaSb semiconductor, Ga and Sb atom pairs pool their valence electrons together, eight electrons for two atoms, and form sp^3 hybrid orbitals with tetrahedral coordination for zinc-blend crystal structure. Commonly, for counting purpose, Ga atoms are thought to be contributing $\frac{3}{4}$ electron toward each bond with Sb atom, while Sb atoms contribute $\frac{5}{4}$ electron toward each bond with Ga atom. Ga atoms on the surface dispense $2 * \frac{3}{4} = \frac{3}{2}$ electrons to bond with Sb atoms in the inner layer. Finding no more Sb atoms to bond with, Ga atoms join together to form dimers, dispensing one additional electron per each

Ga atom. Now we have $\frac{1}{2}$ $(= 3 - 2 * \frac{3}{4} - 1)$ electron left for each atom in Ga-dimers, or one electron in total. Consequently, one of the Ga atoms forms a sp^2-like hybrid orbital (with empty p_z orbital) and gives its $\frac{1}{2}$ electron to the other Ga atom [19, 51, 17, 45, 74]. On the other hand, the other Ga atom forms a sp^3-like hybrid orbital and fills the last dangling bond with one remaining electron. This will create a half-filled sp^3 band and it will cause the Ga-terminating surface to be *weakly metallic* [50]. Consequently, one of the Ga atoms moves down to attain a planar three-fold coordination for itself and tetrahedral four-fold coordination for the other, preferred by sp^2-like and sp^3-like hybrid orbitals, respectively. We observed the angle θ_1 in Fig. 5.6(a) to be 123.8°, clearly showing the two signature characteristics of the sp^2-like hybrid orbitals—planar coordination and 120° bond angles. Bond angle θ_2 in Fig. 5.6(a) was measured to be 99.2°. Although it is distorted slightly beyond the ideal tetrahedral bond angle 109.5°, it certainly shows its preference.

Sb atoms on Sb-terminating surfaces also form dimers in a similar attempt to reduce dangling bonds. We again can count the valence electrons associated with the dimers in similar manners. Out of five of its valence electrons, Sb atoms on the surface dispense $2 * \frac{5}{4} = \frac{5}{2}$ electrons to bond with Ga atoms in the inner layer. The lack of neighbors on the surface causes Sb atoms to join together to form dimers, dispensing one additional electron per each Sb atom. Now we have $\frac{3}{2}$ $(= 5 - 2 * \frac{5}{4} - 1)$ electron left for each atom in Sb-dimers, or three electrons in total. Unlike the case of Ga-dimers, one atom cannot take all three electrons into the last sp^3-like orbital. Thus, both atoms retain their electrons and fill each $\frac{3}{2}$ electrons into the last dangling bond of sp^3-like hybrid orbital. In other words, formation of sp^2-like hybrid orbitals is suppressed because in that case, the remaining $\frac{3}{2}$ electrons must occupy p_z-like band with higher energy, and the band structure energy would be more costly. Therefore, the dimers on Sb-terminating surfaces should be parallel to (001) planes as illustrated in Fig. 5.5. We observed the bond angles θ_1 and θ_2 in Fig. 5.6(b) to be 102.6° and 100.0°, respectively. Wave functions for the unpaired $\frac{3}{2}$ electrons tend to take up more space than those of bonding electrons and cause these angles to be somewhat smaller than the ideal tetrahedral angle 109.5°.

5.5.2 Adsorption of In_2 and As_2 Molecules

In this section, we report the result of our simulations of adsorption of In_2 and As_2 molecules on the surfaces of GaSb semiconductors. We have investigated both the adsorption of In and As atoms and In_2 and As_2 molecules in order to reproduce the experimental deposition process more closely. The added atoms are deposited initially in the form of molecules on the surfaces, but they may break up into individual atoms and settle into different adsorption sites. As mentioned previously in Sec. 5.1, the ultimate purpose of these simulations is to obtain the atomic-scale understanding of the formation of interfaces in III-V heterostructures, such as GaSb/InAs. Therefore, the adsorption of In atoms was done on an Sb-terminating surface, while As atoms were adsorbed on an Ga-terminating surface. These processes simulate the formation of interfaces with two different types of bond types–InSb and GaAs. We use the optimized slab geometries obtained in Sec. 5.5.1 as the starting configurations. These surfaces can have many different reconstructed surface structures depending on the size of the surface unit cells. Obviously, bigger periodic unit cells will produce more variety of complex adsorption patterns. In this report, however, we will consider up to (2×2) surface reconstructions only. Since we are mostly concerned with the adsorption of individual molecules, this unit cell will be adequate to capture the main effects relevant to the interface formation process during molecular beam epitaxy heterostructure crystal growth.

In Fig. 5.6, we show the (2×2) reconstructed Ga- and Sb-terminating surfaces, respectively, viewed from the top. Four most typical lateral locations where we placed the adsorbed atoms initially are also shown. There are second sets of these four adsorption sites (not marked) in the other halves of the unit cells making the total of eight available adsorption sites. We chose the initial height of the adsorbed atom so that the distance to the closest surface atom was the bond length between those atoms in the bulk.

Before we continue, we will define the adsorption sites as labeled in Fig. 5.6(a). We call the site "bridge" (B) site: the As atom is placed over the midpoint of Ga dimers. The site P is called "pedestal" site: the As atom is placed between the two neighboring dimers and above Ga atom in the third top layer. The site C is the "cave" site and the added As atom is placed in the caved region, created by Ga atoms moving away due to dimerization. The site S is called "saddle" site. The Ga atom directly underneath this site has one bond bent upward and another bond bent downward in the perpendicular direction, hence the name. The adsorption sites for In atoms on Sb-terminating surface are labeled in a similar fashion as illustrated in Fig. 5.6(a).

In both cases of bridge (B) and cave (C) sites, the As atom is placed directly above the fourth top layer consisting of Sb atoms. These sites are considered as the “proper” sites because they are the correct places for As atoms to sit if we were to grow an InAs semiconductor film on GaSb substrate with an ideal interface. In the cases of pedestal (P) and saddle (S) sites, on the other hand, As atoms are placed directly above the third top layer consisting of Ga atoms. These sites can be considered as the “wrong” sites because the As atoms on these sites have to move eventually to the “proper” sites in order to grow a new InAs semiconductor film with an ideal interface.

After the atoms to be adsorbed are placed at candidate sites, we relax the entire system–the slab plus the adsorbed atoms. Once the system settles down to an optimized configuration, we calculate the relative energy E_{rel} by comparing the total energy to that of the reference configuration, E_0,

$$E_{rel} = E_{tot} - E_0. \tag{5.1}$$

We choose the configuration with lowest energy (except the ones with inter-atomic exchanges) to be the reference configuration for each surface we study.

Table 5.2 lists relative energies of some of the best adsorption structures for As_2 and In_2 molecules.

Our calculation predicts that As atoms are most likely to be adsorbed at bridge sites on Ga-terminating surfaces. The optimized geometry of the As molecule adsorbed on Ga-terminating surface in the lowest energy configuration is shown in Fig. 5.7.

Table 5.2 Relative energies (in eV) of As_2 and In_2 molecules on Ga- and Sb-terminating surfaces, respectively. The adsorption sites are defined in Fig. 5.6: B-bridge, P-pedestal, C-cave, and S-saddle position. The short-hand notations x, y, and z are the directions the adsorbed molecules are more or less parallel and represent [110], $[1\bar{1}0]$, and [001] directions, respectively. The third group with "exch" suffix represents the configurations with the inter-atomic exchange diffusion. Bold face **0.0** indicates reference configuration.

configuration	As_2	In_2
B+B	**0.0**	0.36
B+P	0.54	0.04
B+C	2.13	0.47
B+S	1.44	0.14
P+P	5.11	**0.0**
P+S	3.14	0.14
C+C	0.74	0.60
C+S	2.48	0.06
S+S	2.32	0.24
P-z	0.50	0.16
C-x	2.47	0.82
B+B exch	**-0.55**	0.62
C+C exch	0.03	0.29

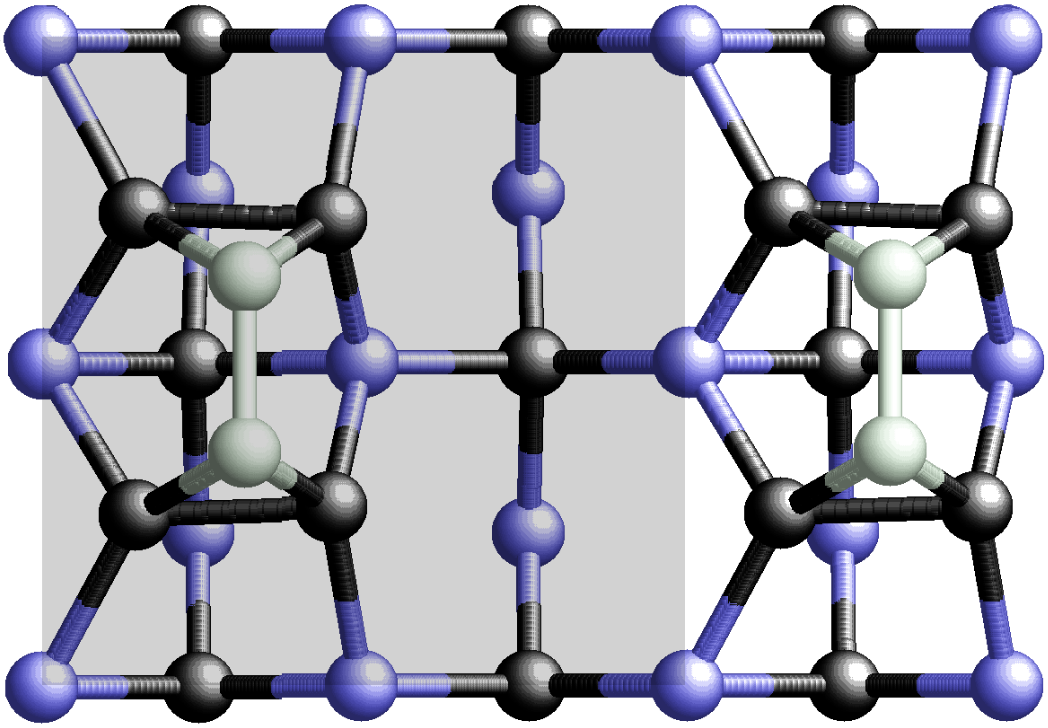

Figure 5.7 The optimized geometry of As atoms adsorbed in the B+B configuration on Ga-terminating surface. Refer the caption of Fig. 5.5 for coloring scheme. White spheres represent the adsorbed As atoms.

The bond length between As and Ga atom is 2.31 Å compared to its bulk value, 2.42 Å [73]. It is worthwhile to note that the adsorption of As atom reversed the trend of buckling: the dimers of Ga atoms are now parallel to (001) planes. Our calculation on In atom adsorption on Sb-terminating surfaces, on the other hand, predicts that there are at least three (possibly four) equally favorable configurations. B+P, B+S, P+P, and C+S configurations have virtually same relative energies for In atom adsorptions. The optimized geometry of the In atoms adsorbed in the reference configuration (P+P) on Sb-terminating surface is shown in Fig. 5.8.

The bond length between In and closest Sb atom is 2.74 Å compared to its bulk value, 2.78 Å [73]. It is a well-known fact that the atoms in molecules or on surfaces bind more tightly. We should also note that As molecules favor the “proper” adsorption sites (see paragraph above for its meaning), bridge sites. Therefore, as next As molecules come in, they will be most likely adsorbed at cave sites. As both bridge and cave sites are occupied by As atoms, the distortion due to dimerization will be completely removed, and an ideal interface will be formed.

The relative energies of adsorption of In molecules on Sb-terminating surfaces seem to predict that In atoms have equal probabilities to be adsorbed in a few different configurations containing both “proper” and “wrong” sites. The relative energies of these configurations are very close. Under the high temperature condition relevant to epitaxial growth process (about 450 $^{\circ}C$), these differences would not have a significant effect. Similar to the case of As molecule adsorption on Ga-terminating surfaces, when the next In

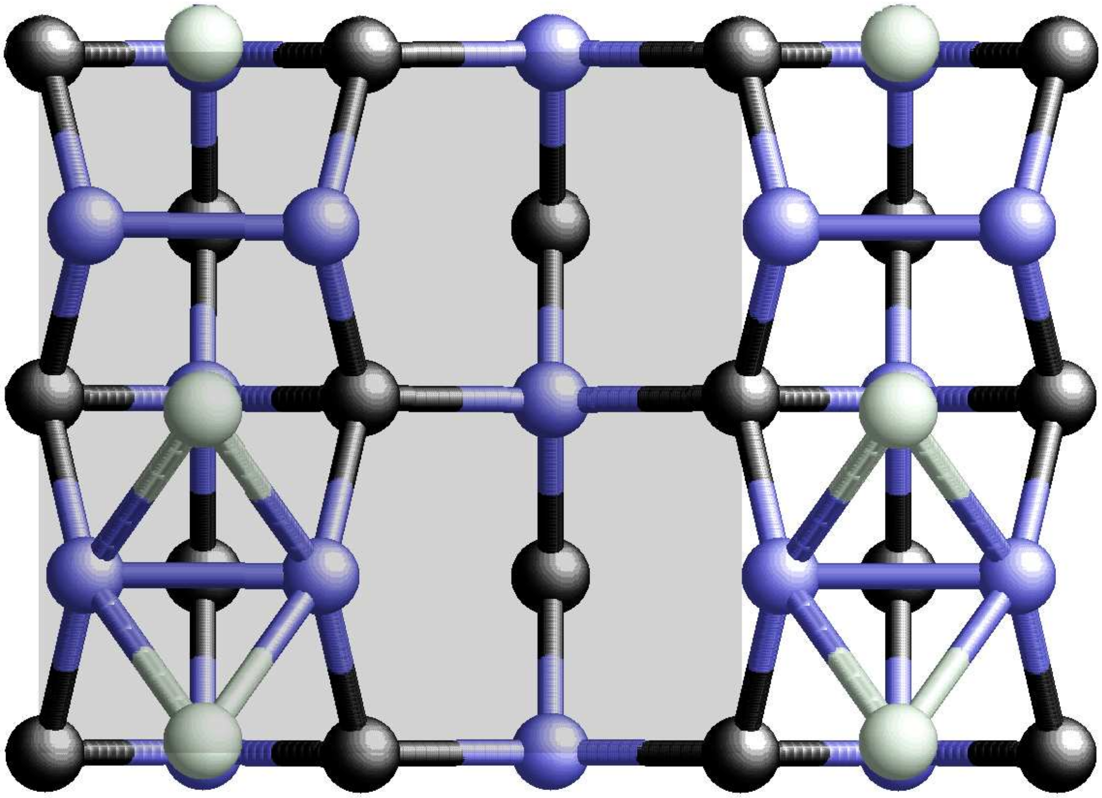

Figure 5.8 The optimized geometry of In atoms adsorbed at in the P+P configuration on Sb-terminating surface. Refer the caption of Fig. 5.5 for coloring scheme. White spheres represent the adsorbed In atoms.

molecule joins in, In atoms are mostly likely to occupy the “proper” sites and defect-free interface will be formed in general.

5.5.3 Inter-atomic Exchange Diffusion

We also investigated the possibility of atomic intermixing during adsorption of As and In molecules. Fig. 5.9 shows the optimized geometry of As molecules adsorbed on Ga-terminating surface and undergone through inter-atomic diffusion.

In this case, As atoms replaced Sb atoms in the second atomic layer from the top and the displaced Sb atoms are in the B+B configuration on Ga-terminating surface. Fig. 5.10 shows the optimized geometry of In molecules adsorbed on Ga-terminating surface and undergone inter-atomic diffusion process.

In this case, In atoms replaced Ga atoms in the second atomic layer from the top and the displaced Ga atoms are in the C+C configuration on Sb-terminating surface. The last group of numbers in Table 5.2 summarizes our results. It is very interesting to note that As-for-Sb exchange on Ga-terminating (001) surface is en exothermic process with the energy gain of more than 0.5 eV. On the contrary, In-for-Ga exchange on Sb-terminating (001) surface is an endothermic process with the energy cost of nearly 0.3 eV. This result is very consistent with the result on the inter-atomic exchange diffusion process in the bulk environment [73]. This difference is also consistent with the experimental observation that interfaces with GaAs-type bonds are typically more disordered than interfaces with InSb-type bonds in InAs/GaSb III-V heterostructures. Furthermore, this result provides

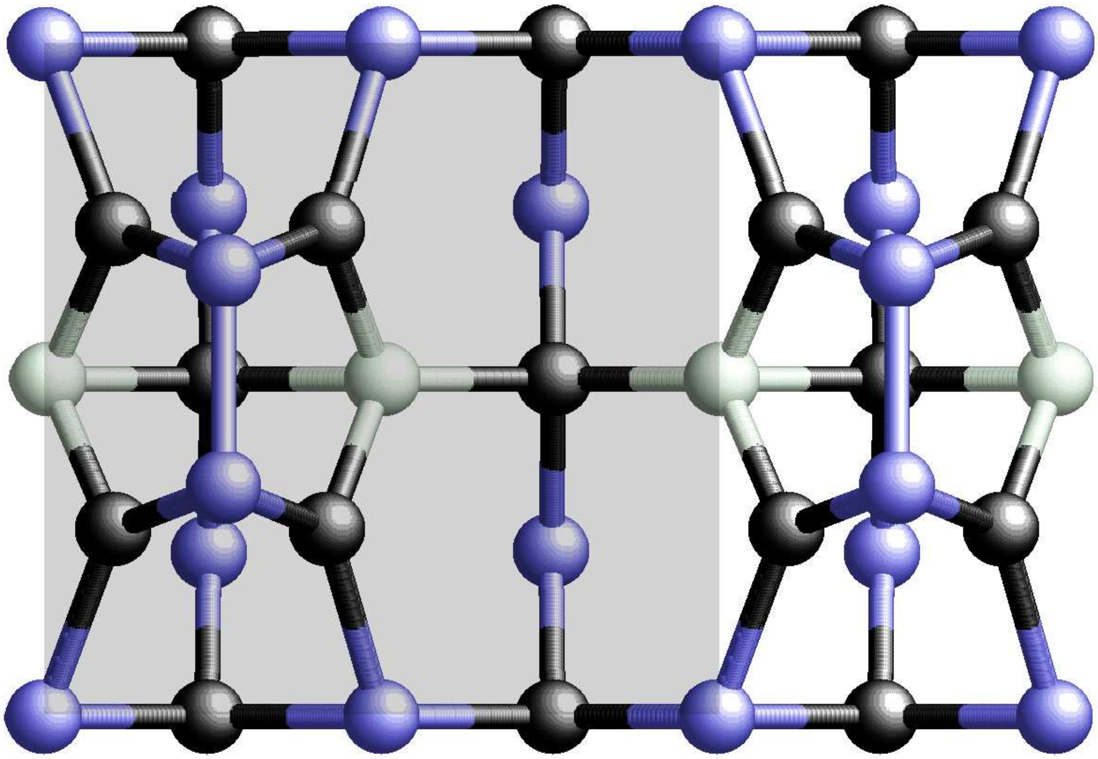

Figure 5.9 The optimized geometry of As-for-Sb inter-atomic diffusion on Ga-terminating surface of GaSb semiconductor. As atoms replaced Sb atoms in the second atomic layer from the top and the displaced Sb atoms are in the B+B configuration on Ga-terminating surface. Refer the caption of Fig. 5.5 for coloring scheme. White spheres represent the adsorbed As atoms.

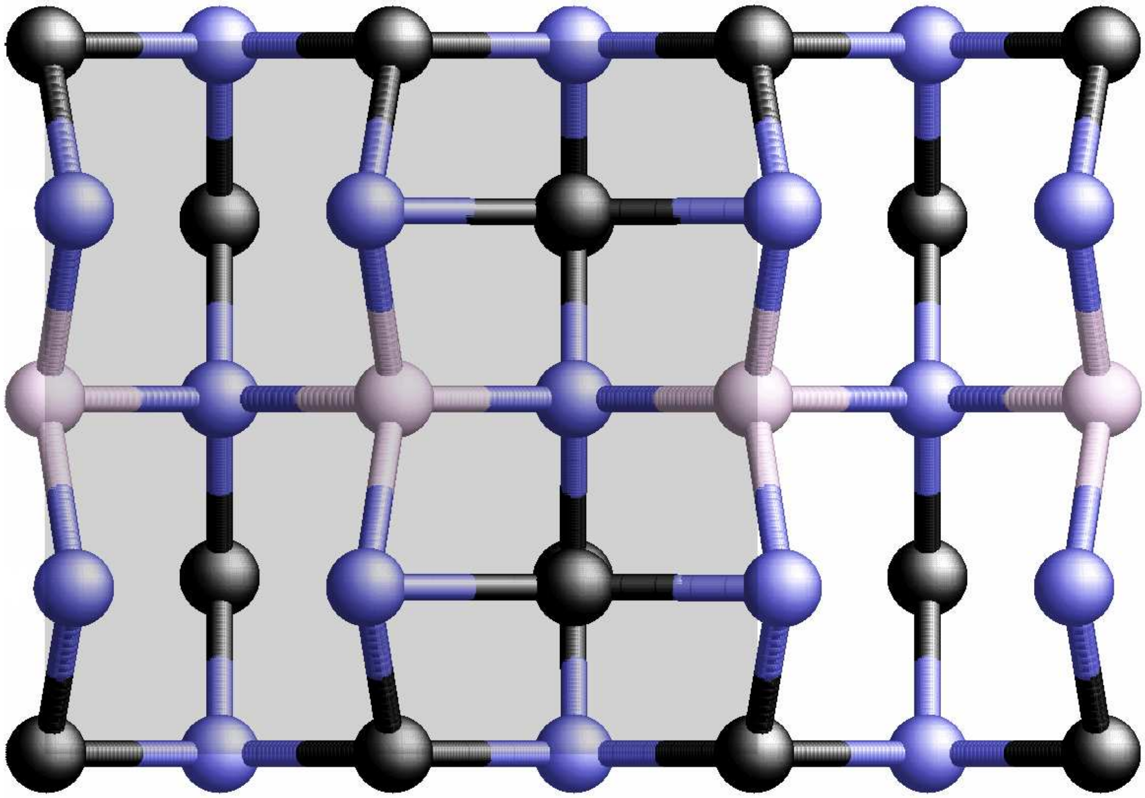

Figure 5.10 The optimized geometry of In-for-Ga inter-atomic diffusion on Sb-terminating surface of GaSb semiconductor. In atoms replaced Ga atoms in the second atomic layer from the top and the displaced Ga atoms are in the C+C configuration on Sb-terminating surface. Refer the caption of Fig. 5.5 for coloring scheme. White spheres represent the adsorbed In atoms.

very strong evidence that the interfacial disorders are caused mainly by the interactomic diffusions occuring during the heterostructure growth process.

To give a complete and definite argument, however, a more complete study involving the kinetic effect and barrier estimation by identifying the minimum energy reaction path. A further research along this line will provide valuable information in attaining the complete understanding of interface formation during molecular beam epitaxy (MBE) heterostructure growth.

5.6 Summary

In summary, we have used first-principles electronic-structure methods to clarify the interpretation of XSTM images of (110) surfaces on cleaved InAs/GaSb heterostructures, focusing on the differences between interfaces with InSb versus GaAs bonds. We find that the apparent height differences between the InAs and GaSb surfaces are largely associated with the electronic structure, whereas the local height differences at the InSb and GaAs interfaces are caused by geometric relaxation from the partial relief of local bond strain. We also investigated the atomistic process relevant to the formation of GaAs and InSb bond-type interfaces: the adsoprtion of In or As atoms on (001) surfaces of GaSb semiconductors. We observed that both Ga- and Sb-terminating surfaces showed dimerization of surface atoms. One of the Ga atoms of the dimers formed sp^2 hybrid orbitals while the other formed sp^3 hybrid orbitals. This caused Ga-dimers to tilt out of the (001) planes and the Ga-terminating surface to buckle. On the other hand, both atoms in Sb dimers formed sp^3 hybrid orbitals and consequently the Sb-terminating surfaces did not show any buckling. Our calculations also predict that arsenic atoms would be preferably adsorbed at the bridge site between the dimerized Sb atoms on Sb-terminating (001) surfaces. Indium atoms, on the other hand, were observed to have somewhat equal probabilities to be adsorbed at several different sites on Ga-terminating (001) surfaces. When In atom was adsorbed on Ga-dimers, we observed that the surface buckling was nullified and the dimers reverted back to horizontal positions. Finally, our calculations of the energies associated with interfacial exchange of anions reveal that As-for-Sb exchanges on Ga-terminating surfaces are exothermic at GaAs bond-type interfaces, but In-for-Ga exchanges on Sb-terminating surfaces are endothermic at InSb bond-type interfaces. This result is consistent with the experimental observation that GaAs bond-type interfaces are typically more disordered than InSb bond-type interfaces in the InAs/GaSb heterostructures.

CHAPTER VI

CONCLUSIONS

In this dissertation we studied the surfaces of metals and semiconductors, particularly palladium and III-V semiconductors, by using first-principle calculation method based on density functional theory. Our main results can be summarized as follows.

In the first principle calculations of metal surfaces, we determined the ground-state structure of two-vacancy defect of H atom on Pd(111) surface by treating the motion of a H atom quantum mechanically in the vicinity of the defect. We solved Schrödinger equation for a single H atom moving in static potential energy surface that has been mapped out by first-principles density-functional theory calculations. We find that a H atom in the vicinity of a two-vacancy defect experiences substantial quantum effects and its wave functions are delocalized over large portion of the defect. Our results indicate that the ground-state wave function is concentrated in the hcp site rather than the fcc site where H atoms normally settle on Pd(111) surfaces. We show that symmetry plays a major role in the reversal of the order of the most enegetically favorable sites. Our results explain the STM images of two- and multi-vacancy defects with ground-state properties of the defects. More importantly, our model also provides a compelling argument in elucidating the high activity of three-or larger defects in hydrogen molecule dissociation and the inactivity of a two-vacancy defect.

In the first principle calculations of semiconductor surfaces, we determined that the apparent height differences between the InAs and GaSb surfaces are largely associated with the electronic structure, whereas the local height differences at the InSb and GaAs interfaces are caused by geometric relaxation from the partial relief of locl bond strain. Both Ga- and Sb-terminating surfaces show dimerization of surface atoms. One of the Ga atoms of the dimers formed sp^2 hybrid orbitals while the other formed sp^3 hybrid orbitals. This causes Ga dimers to tilt out of the (001) planes and the Ga-terminating surface to buckle. On the other hand, both atoms in Sb dimers formed sp^3-hybrid orbitals and consequently the Sb-terminating surfaces does not show any buckling. Our calculations also predict that arsenic atoms would be preferably adsorbed at the bridge site between the dimerized Sb atoms on Sb-terminating (001) surfaces. Indium atoms, on the other hand, are observed to have somewhat equal probabilities to be adsorbed at several different sites on Ga-terminating (001) surfaces. When an In atom is adsorbed on Ga dimers, we observe that the surface buckling is nullified and the dimers revert back to horizontal positions. Our calculations of the energies associated with interfacial exchange of anions reveal that As-for-Ga exchanges on Sb-terminating surfaces are endothermic at InSb bond-type interfaces. This result is consistent with the experimental observation that GaAs bond-type interfaces are typically more disordered than InSb bond-type interfaces in the InAs/GaSb heterostructures.

REFERENCES

[1] A. R. Smith, K.-J. Chao, C. K. Shih, Y. C. Shih, K. A. Anselm, and B. G. Streetman, "Influence of various growth parameters on the interface abruptness of AlAs/GaAs short period superlattices," *J. Vac. Sci. Technol. B*, vol. 13, 1995, pp. 1824–1829.

[2] A. T. Haug, R. E. White, J. W. Weidner, W. Huang, S. Shi, T. Stoner, and N. Rana, "Increasing Proton Exchange Membrane Fuel Cell Catalyst Effectiveness Through Sputter Deposition," *J. Electrochem. Soc.*, vol. 149, 2002, pp. A280–A287.

[3] A.C. Luntz, J.K. Brown, and M. D. Williams, "Molecular beam studies of H2 and D2 dissociative chemisorption on Pt(111)," *J. Chem. Phys.*, vol. 93, no. 7, 1990, pp. 5240–5246.

[4] N. W. Ashcroft and N. D. Mermin, *Solid State Physics*, Holt, Rinehart and Winston, New York, 1976.

[5] B. Brar, J. Ibbetson, H. Kroemer, and J.H. English, "Effects of the Interface Bonding Type on the Optical and Structural-Properties of InAs-AlSb Quantum-Wells," *Appl. Phys. Lett.*, vol. 64, 1994, pp. 3392–3394.

[6] B. Z. Nosho and B. R. Bennett and L. J. Whitman and M. Goldenberg, "Effects of As_2 versus As_4 on InAs/GaSb heterostructures: As-for-Sb exchange and film stability," *J. Vac. Sci. Technol. B*, vol. 19, 2001, pp. 1626–1630.

[7] G. B. Bachelet, D. R. Hamann, and M. Schlüter, "Pseudopotentials that work: From H to Pu," *Phys. Rev. B*, vol. 26, no. 8, 1982, pp. 4199–4228.

[8] G. B. Bachelet, D. R. Hamann, and M. Schlüter, "Pseudopotential study of binding properties of solids within generalized gradient approximations: The role of core-valence exchange correlation," *Phys. Rev. B*, vol. 57, no. 4, 1998, pp. 2134–2145.

[9] B.J.J. Koeleman, T. de Zwart, and A. L. Boers, "Information on Adsorbate Positions from Low-Energy Recoil Scattering: Adsorption of Hydrogen on Pt," *Phys. Rev. Lett.*, vol. 56, 1986, pp. 1152–1155.

[10] B.R. Bennett, B.V. Shanabrook, and E.R. Glaser, "Interface Control in InAs/AlSb Superlattices," *Appl. Phys. Lett.*, vol. 65, 1994, pp. 598–600.

[11] E. L. Briggs, D. J. Sullivan, and J. Bernholc, "Real-space multigrid-based approach to large-scale electronic structure calculations," *Phys. Rev. B*, vol. 54, no. 20, 1996, pp. 14362–14375.

[12] C. Kittel, *Introduction to Solid State Physics*, Addison-Wesley, Reading, MA, 1986.

[13] M. Côté, J. C. Grossman, M. L. Cohen, and S. G. Louie, "Electron-phonon interactions in solid C_{36}," *Phys. Rev. Lett.*, vol. 81, 1998, pp. 697–700.

[14] D. M. Bruls, J. W. A. M. Vugs, P. M. Koenraad, H. W. M. Salemink, J. H. Wolter, M. Hopkinson, M. S. Skolnick, F. Long, and S. P. A. Gill, "Determination of the shape and indium distribution of low-growth-rate InAs quantum dots by cross-sectional scanning tunneling microscopy," *Appl. Phys. Lett.*, vol. 81, no. 9, 2002, pp. 1708–1710.

[15] D. M. Ceperley and B. J. Alder, "Ground State of the Electron Gas by a Stochastic Method," *Phys. Rev. Lett.*, vol. 45, 1980, pp. 566–569.

[16] David Vanderbilt, "Soft self-consistent pseudopotentials in a generalized engenvalue formalism," *Phys. Rev. B*, vol. 41, 1990, pp. 7892–7895.

[17] C. B. Duke, A. R. Lubinsky, B. W. Lee, and P. Mark, "Atomic geometry of cleavage surfaces of tetrahedrally coordinated compound semiconductors," *J. Vac. Sci. Technol.*, vol. 13, no. 4, 1976, pp. 761–768.

[18] P. Ebert, "Nano-scale properties of defects in compound semiconductor surfaces," *Surf. Sci. Rep.*, vol. 33, 1999, pp. 121–303.

[19] B. Engels, P. Richard, K. Schroeder, S. Blügel, P. Ebert, and K. Urban, "Comparision between *ab initio* theory and scanning tenneling microscopy for (110) surfaces of III-V semiconductors," *Phys. Rev. B*, vol. 58, 1998, pp. 7799–7815.

[20] E.R. Brown, J.R. Söderström, C.D. Parker, L.J. Mahoney, K.M. Molvar, and T.C. McGill, "Oscillations up to 712 Ghz in InAs/AlSb Resonant-Tunneling Diodes," *Appl. Phys. Lett.*, vol. 58, 1991, pp. 2291–2293.

[21] F. Fuchs, U. Weimer, W. Pletschen, J. Schmitz, E. Ahlswede, M. Walther, J. Wagner, and P. Koidl, "High performance InAs/$Ga_{1-x}In_xSb$ superlattice infrared photodiodes," *Appl. Phys. Lett.*, vol. 71, 1997, pp. 3251–3253.

[22] R. M. Feenstra and J. A. Stroscio, "Tunneling spectroscopy of the GaAs(110) surface," *J. Vac. Sci. Technol. B*, vol. 5, 1987, pp. 923–929.

[23] R. P. Feynman, "Forces in Molecules," *Phys. Rev.*, vol. 56, no. 4, 1939, pp. 340–343.

[24] G. Kresse and J. Furthmüller, "Efficient iterative schemes for *ab initio* total-energy calculations using a plane-wave basis set," *Phys. Rev. B*, vol. 54, 1996, pp. 11169–11186.

[25] G. Kresse and J. Hafner, "Ab initio molecular dynamics for liquid metals," *Phys. Rev. B*, vol. 47, no. 1, 1993, pp. 558–561.

[26] G. Kresse and J. Hafner, "Norm-conserving and ultrasoft pseudopotentials for first-row and transition elements," *J. Phys.: Condens. Matter*, vol. 6, 1994, pp. 8245–8257.

[27] G. Papoian, J. K. Norskov, and R. Hoffmann, "Adsorption energies and ordered structures of hydrogen on Pd(111) from density-functional periodic calculations," *Phys. Rev. B*, vol. 58, 1998, pp. 10890–10898.

[28] G. Tuttle, H. Kroemer, and J.H. English, "Effects of Interface Layer Sequencing on the Transport-Properties of InAs/AlSb Quantum-Wells - Evidence for Antisite Donors at the InAs/AlSb Interface," *J. Appl. Phys.*, vol. 67, 1990, pp. 3032–3037.

[29] S. Goedecker, M. Teter, and J. Hutter, "Separable dual-space Gaussian pseudopotentials," *Phys. Rev. B*, vol. 54, no. 3, 1996, pp. 1703–1710.

[30] X. Gonze, P. Käckell, and M. Scheffler, "Ghost states for separable, norm-conserving, ab initio pseudopotentials," *Phys. Rev. B*, vol. 41, no. 17, 1990, pp. 12264–12267.

[31] Gustav Källén and Göran Wahnström, "Quantum treatment of H adsorbed on a Pt(111) surface," *Phys. Rev. B*, vol. 65, 2002, p. 033406 [4 pages].

[32] D. R. Hamann, M. Schlüter, and C. Chiang, "Norm-Conserving Pseudopotentials," *Phys. Rev. Lett.*, vol. 43, no. 20, 1979, pp. 1494–1497.

[33] J. Harper, M. Weimer, D. Zhang, C.-H. Lin, and S. S. Pei, "Cross-sectional scanning tunneling microscopy characterization of molecular beam epitaxy grown InAs/GaSb/AlSb heterostructures for mid-infrared interband cascade lasers," *J. Vac. Sci. Technol. B*, vol. 16, 1998, pp. 1389–1394.

[34] J. F. Paul and P. Sautet, "Comparison of the nature of the hydrogen-metal bond on Pd(111) and Ni(111) by a periodic density functional method," *Surf. Sci.*, vol. 356, 1996, pp. L403–L409.

[35] J. Ihm, A. Zunger, and L. M. Cohen, "Momentum-space formalism for the total energy of solids," *J. Phys. C: Solid State Phys.*, vol. 12, 1979, pp. 4409–4422.

[36] J. P. Perdew and A. Zunger, "Self-interaction correction to density-functional approximations for many-electron systems," *Phys. Rev. B*, vol. 23, 1981, pp. 5048–5079.

[37] J. Steinshnider, M. Weimer, R. Kaspi, and G. W. Turner, "Visualizing Interfacial Structure at Non-Common-Atom Heterojunctions with Cross-Sectional Scanning Tunneling Microscopy," *Phys. Rev. Lett.*, vol. 85, no. 14, 2000, pp. 2953–2956.

[38] J. D. Jackson, *Classical Electrodynamics*, J. Wiley and Sons, New York, 1975.

[39] J.B. Boos, W. Kruppa, B.R. Bennett, D. Park, S.W. Kirchoefer, R. Bass, and H.B. Dietrich, "AlSb/InAs HEMT's for low-voltage, high-speed applications," *IEEE Trans. Electron Devices*, vol. 45, 1998, pp. 1869–1875.

[40] R. O. Jones and O. Gunnarsson, "The density functional formalism, its applications and prospects," *Rev. Mod. Phys.*, vol. 61, no. 3, Mar. 1989, pp. 689–746.

[41] J.S. Scott, J.P. Kaminski, S.J. Allen, D.H. Chow, M. Lui, and T.Y. Liu, "Terahertz Response of Resonant-Tunneling Diodes," *Surf. Sci.*, vol. 305, 1994, pp. 389–392.

[42] K. Christmann, "Interaction of hydrogen with solid-surfaces," *Surf. Sci. Rep.*, vol. 9, 1988, pp. 1–163.

[43] K. Christmann, R. J. Behm, G. Ertl, M. A. Vanhove, and W. H. Weinberg, "Chemisorption geometry of hydrogen on Ni(111) - Order and disorder," *J. Chem. Phys.*, vol. 70, 1979, pp. 4168–4184.

[44] K. Umezawa, T. Ito, M. Asada, S. Nakanishi, P. Ding, W. A. Lanford, and Hjörvarsson, "Adsorption of hydrogen on the Pt(111) surface from low-energy recoil scattering," *Surf. Sci.*, vol. 387, 1997, pp. 320–327.

[45] A. Kahn, "Semiconductor surface structures," *Surf. Sci. Rep.*, vol. 3, 1983, pp. 193–300.

[46] L. Kleinman and D. M. Bylander, "Efficacious Form for Model Pseudopotentials," *Phys. Rev. Lett.*, vol. 48, no. 20, May 1982, pp. 1425–1428.

[47] K.M. Lui, Y. Kim, W. M. Lau, and J. W. Rabalais , "Adsorption site determination of light elements on heavy substrates by low-energy ion channeling," *J. Appl. Phys.*, vol. 86, 1999, pp. 5256–5262.

[48] W. Kohn and L. J. Sham, "Self-consistent Equations Including Exchange and Correlation Effects," *Phys. Rev.*, vol. 140, 1965, pp. A1133–A1138.

[49] K.P. Huber and G. Herzberg, *Molecular Spectra and Molecular Structure, Constants of Diatomic Molecules*, vol. 4, Van Norstrand-Reinhold, New York, 1979.

[50] L.J. Whitman, P.M. Thibado, S.C. Erwin, B.R. Bennett, and B.V. Shanabrook, "Metallic III-V (001) Surfaces: Violations of the Electron Counting Model," *Phys. Rev. Lett.*, vol. 79, 1997, pp. 693–696.

[51] A. R. Lubinsky, C. B. Duke, B. W. Lee, and P. Mark, "Semiconductor Surface Reconstruction: The Rippled Geometry of GaAs(110)," *Phys. Rev. Lett.*, vol. 36, 1976, pp. 1058–1061.

[52] M. C. Payne, M. P. Teter, D. C. Allan, T. A. Arias, and J. D. Joannopoulos, "Iterative minimization techniques for *ab initio* total-energy calculations: molecular dynamics and conjugate gradients," *Rev. Mod. Phys.*, vol. 64, 1992, pp. 1045–1097.

[53] M. J. Puska, R. M. Nieminen, M. Manninen, B. Chakraborty, S. Holloway, and J. K. Norskov, "Quantum Motion of Chemisorbed Hydrogen on Ni Surfaces," *Phys. Rev. Lett.*, vol. 51, 1983, pp. 1081–1084.

[54] C. Mailhiot, C. B. Duke, and D. J. Chadi, "Sb overlayers on (110) surfaces of III-V semiconductors: Total-energy minimization and surface electronic structure," *Phys. Rev. B*, vol. 31, 1985, pp. 2213–2229.

[55] M.J. Yang, W.J. Moore, B.R. Bennett, and B.V. Shanabrook, "Growth and characterisation of InAs/InGaSb/InAs/AlSb infrared laser structures," *Electron. Lett.*, vol. 34, 1998, pp. 270–272.

[56] B. Z. Nosho, W. Barvosa-Carter, M. J. Yang, B. R. Bennett, and L. J. Whitman, "Interpreting interfacial structure in cross-sectional STM images of III-V semiconductor heterostructures," *Surf. Sci.*, vol. 465, 2000, pp. 361–371.

[57] Nuria Lopez, Zbigniew Lodziana, Francesc Illas, and M. Salmeron, "When Langmuir Is Too Simple: H_2 Dissociation on Pd(111) at High Coverage," *Phys. Rev. Lett.*, vol. 93, 2004, p. 146103 [4 pages].

[58] O. Albrektsen, D. J. Arent, H. P. Meier, and H. W. M. Salemink, "Tunneling microscopy and spectroscopy of molecular beam epitaxy grown GaAs-AlGaAs interfaces," *Appl. Phys. Lett.*, vol. 57, no. 1, 1990, pp. 31–33.

[59] O. M. Lovvik and R. A. Olsen, "Adsorption energies and ordered structures of hydrogen on Pd(111) from density-functional periodic calculations," *Phys. Rev. B*, vol. 58, 1998, pp. 10890–10898.

[60] P. Ordejón, E. Artacho, , and J. M. Soler., "Self-consistent order-N density-functional calculations for very large systems," *Phys. Rev. B*, vol. 53, no. 16, 1996, pp. R10441–R10444.

[61] P. Ordejón, D. A. Drabold, R. M. Martin, and M. P. Grumbach, "Linear system-size scaling methods for electronic-structure calculations," *Phys. Rev. B*, vol. 51, 1995, pp. 1456–1476.

[62] P. Hohenberg and W. Kohn, "Inhomogeneous Electron Gas," *Phys. Rev.*, vol. 136, 1964, pp. B864–B871.

[63] P. J. Feibelman and D. R. Hamann, "Theory of H-bonding and vibration on Pt(111)," *Surf. Sci.*, vol. 182, 1987, pp. 411–422.

[64] R. G. Parr and W. Yang, *Density-Functional Theory of Atoms and Molecules*, Oxford University Press, 1989.

[65] J. P. Perdew, K. Burke, and M. Ernzerhof, "Generalized Gradient Approximation Made Simple," *Phys. Rev. Lett.*, vol. 77, no. 18, 1996, pp. 3865–3868.

[66] R. A. Olsen, G. J. Kroes, and E. J. Baerends, "Atomic and molecular hydrogen interacting with Pt(111)," *J. Chem. Phys.*, vol. 111, 1999, pp. 11155–11163.

[67] R. M. Feenstra, D. A. Collins, D. Z. Y. Ting, M. W. Wang, and T. C. McGill, "Interface roughness and asymmetry in InAs/GaSb superlattices studied by scanning tunneling microscopy," *Phys. Rev. Lett.*, vol. 72, no. 17, 1994, pp. 2749–2752.

[68] S. C. Badescu, P. Salo, T. Ala-Nissila, S. C. Ying, K. Jacobi, Y. Wang, K. Bedurftig, and G. Ertl, "Energetics and vibrational states for hydrogen on Pt(111)," *Phys. Rev. Lett.*, vol. 88, 2002, p. 136101 [4 pages].

[69] S. C. Badescu, S. C. Ying, and T. Ala-Nissila, "Quantum diffusion of H/Ni(111) through a Monte Carlo wave function formalism," *Phys. Rev. Lett.*, vol. 86, 2001, pp. 5092–5095.

[70] S. Gwo, K.-J. Chao, C. K. Shih, K. Sadra, and B. G. Streetman, "Direct mapping of electronic structure across $Al_{0.3}Ga_{0.7}As$/GaAs heterojunctions: Band offsets, asymmetrical transition widths, and multiple-valley band structures," *Phys. Rev. Lett.*, vol. 71, no. 12, 1993, pp. 1883–1886.

[71] S. L. Zuo, Y. G. Hong, E. T. Yu, and J. F. Klem, "Cross-sectional scanning tunneling microscopy of GaAsSb/GaAs quantum well structures," *J. Appl. Phys.*, vol. 92, no. 7, 2002, pp. 3761–3770.

[72] S. Y. Cha and W. M. Lee, "Performance of proton exchange membrane fuel cell electrodes prepared by direct deposition of ultrathin platinum on the membrane surface," *J. Electrochem. Soc.*, vol. 146, 1999, pp. 4055–4060.

[73] S.G. Kim, S.C. Erwin, B.Z. Nosho, and L.J. Whitman, "Electronic versus geometric contrast in cross-sectional STM images of III-V semiconductor heterostructures," in press, 2003.

[74] C. A. Swarts, T. C. McGill, and W. A. G. III, "Reconstruction of the (110) surface of III-V semiconductor compounds," *Surf. Sci.*, vol. 110, 1981, pp. 400–414.

[75] T. E. Felter, E. C. Sowa, and M. A. Van Hove, "Location of hydrogen adsorbed on palladium (111) studied by low-energy electron diffraction," *Phys. Rev. B*, vol. 40, 1989, pp. 891–899.

[76] T. Mitsui, M. K. Rose, E. Fomin, D. F. Ogletree, and M. Salmeron, "Dissociative hydrogen adsorption on palladium requires aggregates of three or more vacancies," *Nature*, vol. 422, 2003, pp. 705–707.

[77] T. Mitsui, M. K. Rose, E. Fomin, D. F. Ogletree, and M. Salmeron, "Hydrogen adsorption and diffusion on Pd(111)," *Surf. Sci.*, vol. 540, 2003, pp. 5–11.

[78] J. Tersoff and D. R. Hamann, "Theory and Application for the Scanning Tunneling Microscope," *Phys. Rev. Lett.*, vol. 50, 1983, p. 1998.

[79] V. Pallassana, M. Neurock, L. B. Hansen, B. Hammer, and J. K. Norskov, "Theoretical analysis of hydrogen chemisorption on Pd(111), Re(0001) and Pd-ML/Re(0001), Re-ML/Pd(111) pseudomorphic overlayers," *Phys. Rev. B*, vol. 60, 1999, pp. 6146–6154.

[80] W. Barvosa-Carter, A.S. Bracker, J.C. Culbertson, B.Z. Nosho, B.V. Shanabrook, L.J. Whitman, Hanchul Kim, N.A. Modine, and E. Kaxiras, "Structure of III-Sb(001) Growth Surfaces: The Role of Heterodimers," *Phys. Rev. Lett.*, vol. 84, 2000, pp. 4649–4652.

[81] W. Dong and J. Hafner, "H_2 dissociative adsorption on Pd(111)," *Phys. Rev. B*, vol. 56, 1997, pp. 15396–15403.

[82] Z. Zhang and M.G. Lagally, "Atomistic processes in the early stages of thin-film growth," *Science*, vol. 276, 1997, pp. 377–383.